UC Merced
UC Merced Electronic Theses and Dissertations

Title
Electrical Contact Resistance at Sub-micron Interfaces Investigated via Conductive Atomic Force Microscopy

Permalink
https://escholarship.org/uc/item/14s4z8v1

Author
Sumaiya, Saima Aktar

Publication Date
2020

Peer reviewed|Thesis/dissertation

eScholarship.org Powered by the California Digital Library
University of California

UNIVERSITY OF CALIFORNIA, MERCED

Electrical Contact Resistance at Sub-micron Interfaces Investigated via Conductive Atomic Force Microscopy

A Thesis submitted in partial satisfaction of the requirements
for the degree of Master of Science

in

Mechanical Engineering

by

Saima Aktar Sumaiya

Committee in charge:

Professor Mehmet Z. Baykara, Chair
Professor Ashlie Martini
Professor Venkattraman Ayyaswamy

Dec 2020

Portion of Chapter 2 © 2019 AIP Publishing
Portion of Chapter 3 © 2020 IOP Publishing

All other chapters
© Saima Aktar Sumaiya, 2020
All rights are reserved.

This Thesis of Saima Aktar Sumaiya is approved, and it is acceptable in quality and form for publication on microfilm and electronically:

Mehmet Z. Baykara, Chair	Date
Ashlie Martini	Date
Venkattraman Ayyaswamy	Date

University of California, Merced

Dec 2020

To My Loving Parents

ACKNOWLEDGMENT

First of all, I would like to express my sincere gratitude to my advisor, Prof. Mehmet Baykara for his continued support and guidance. Prof. Baykara's knowledge and encouragement enabled me to overcome the various hurdles I faced in my research. His insightful recommendations and mentoring shaped my research outlook. His guidance and feedback helped me in writing this thesis. I am thankful to Prof. Baykara for giving me opportunities to develop professional skills. Besides that, I find solace in his continued care for my personal well being. I am privileged to work with such a kind and supportive mentor.

I am also thankful to Prof. Ashlie Martini and Prof. Venkattraman Ayyaswamy for being in my thesis committee and their support.

My sincere thanks go to the Air Force Office of Scientific Research and the Molecular Foundry at Lawrence Berkeley National Laboratory for supporting my research.

I would also like to extend my appreciation to my fellow Baykara lab members, namely Ogulcan Acikgoz, Wai Oo, Mohammad Jaman and Anthony Rodriguez for their support and help. I feel lucky to work with such friendly and respectful lab members.

I cannot thank enough my partner, Shiekh Zia Uddin for always being there for me. I have always found a sympathetic ear in him during the ups and downs of my research. I would not be in the position where I am today without my parents' support. I would like to express my gratitude to them for their constant belief in me. I am grateful to my parents for raising me as an independent woman and always being respectful regarding my decisions. I also cannot deny the constant support and encouragement I received from my friends, especially from Lauren Miklose and Shrishail Baligar.

ABSTRACT

Electrical contact resistance (ECR) is an important parameter to optimize the design and, evaluate the contact reliability and performance of small-scale electrical and electro-mechanical systems including those that are implemented in crucial radar and telecommunication technologies. State-of-the art electronic devices utilizing metal-insulator-metal or molecular tunnel junctions are also affected to a great extent by ECR. Consequently, it is of utmost importance to understand the physical mechanisms pertinent to ECR and to precisely characterize ECR at different types of interfaces formed between mating surfaces.

In this thesis, we primarily focused on measuring ECR at atomically flat, sub-micron interfaces formed between gold islands and highly oriented pyrolytic graphite (HOPG) via conductive atomic force microscopy (C-AFM). By means of proof-of-principle experiments, we were able to correlate the measured ECR in the diffusive conduction regime (where contact size is larger than the electron mean free path) to *true*, measurable contact areas. We also presented an improved approach that led to more reliable ECR measurements via C-AFM by suppressing the effects of tip deformation, humidity and temperature variations as well as substrate roughness on the experiments. The ECR values measured via this improved technique follow a Gaussian distribution with a much lower standard deviation compared to those obtained via conventional approaches. Finally, we demonstrated an improved method to synthesize gold islands of varying size on HOPG that can be utilized in future research to investigate the physical mechanisms of ECR in the intermediate conduction regime whereby the contact size is on the order of the electron mean free path.

In summary, the findings reported in this thesis constitute the first measurements of ECR in the diffusive conduction regime as a function of true contact area at atomically flat interfaces. Based on crucial improvements in sample synthesis and measurement methodology reported in this thesis, future work will focus on elucidating the physical mechanisms of ECR across all electron conduction regimes.

TABLE OF CONTENTS

ACKNOWLEDGMENT . . . . **ii**
ABSTRACT . . . . **iii**
LIST OF FIGURES . . . . **vi**
LIST OF TABLES . . . . **x**

1 INTRODUCTION **1**

1.1 Electrical Contact Resistance 1
1.2 Atomic Force Microscopy 4

1.2.1 General Operating Principle of AFM 5
1.2.2 Contact-Mode AFM 5
1.2.3 Dynamic Modes of AFM 7
1.2.4 Force Spectroscopy via AFM 8

1.3 Conductive Atomic Force Microscopy 8
1.4 Research Objectives 9
1.5 Thesis Outline 10

2 ELECTRICAL CONTACT RESISTANCE AT ATOMICALLY FLAT INTERFACES **11**

2.1 Electrical Contact Resistance and Contact Area 11
2.2 Materials and Methods 12
2.3 Results and Discussion 14

2.3.1 Correlation between Island Size and Total ECR 14
2.3.2 Extracting the ECR at the Island-HOPG Junction 16

2.4 Summary 20

3 IMPROVING THE RELIABILITY OF ECR MEASUREMENTS 21

3.1 Reliability of ECR Measurements 21
3.2 Materials and Methods 22
3.3 Results and Discussion 23

3.3.1 Comparison between Conventional and Improved ECR Measurements 23
3.3.2 Spontaneous Changes in ECR Measurements 26

3.4 Summary 28

4 IMPROVED SYNTHESIS OF GOLD ISLANDS ON GRAPHITE 30

4.1 Complexities of Gold Island Synthesis on Graphite 30
4.2 Materials and Methods 31
4.3 Results and Discussion 32

4.3.1 Optimizing Synthesis Parameters 32
4.3.2 Electrical Contact Resistance in Different Conduction Regimes 34

4.4 Summary 36

5 CONCLUSIONS 37

BIBLIOGRAPHY 39

LIST OF FIGURES

1.1 Schematic of surface roughness on different sampling lengths. 1

1.2 A schematic showing constriction of electrical current lines at "a-spots" formed between asperities of two surfaces in contact. 2

1.3 Schematic of a representative MEMS device with electrical contacts. Figure from Ref. [7]. 3

1.4 Schematic of a typical AFM. 6

1.5 Schematic of tip-sample interaction force (F) as a function of separation distance (d). 7

1.6 Different operational modes of AFM: (a) contact mode, (b) intermittent contact (i.e. tapping) mode and (c) non-contact mode. 7

2.1 Representative SEM image of (a) thin gold film thermally evaporated on freshly cleaved HOPG, (b) the sample system consisting of gold islands of varying size on HOPG, obtained via annealing of the sample in (a). 13

2.2 AFM image of several gold islands on HOPG. Two gold islands (of size 34,800 nm^2 and 111,900 nm^2) on which I-V measurements were performed are highlighted with dashed circles and indicated as (i) and (ii), respectively. 13

2.3 (a) Five I-V curves obtained on an individual spot on island (i) in Figure 2.2 over a duration of 2 min., demonstrating high reproducibility. Note that the current saturates at 20.0 nA, which is the limit of our measurement setup. (b) Five I-V curves obtained on five different spots on island (i) in Figure 2.2, demonstrating noticeable variability. (c) Five I-V curves obtained on five different spots on island (ii) in Figure 2.2, demonstrating less variability than those obtained on island (i). Please note the larger slope of the I-V curves on island (ii) when compared with island (i), indicative of a smaller resistance to electron flow, in accordance with the larger size of the island. 15

2.4 (a) Perspective view of the MD simulations where a model AFM tip apex comes into contact with gold islands of varying size on a graphite substrate. (b) For each tip-island combination, current between the tip and the edge of the graphite substrate (shown in darker gray) is approximated using the EChemDID method. 17

2.5 Total resistance calculated from the simulations as a function of island radius for three different model tips (symbols). The data are fit to an exponential function (dashed lines) to determine the maximum island radius for each tip (arrows), after which the contribution of the island-HOPG resistance to the total resistance becomes negligible (see the text). Inset: Maximum island radius for each model tip (considering island radii where the total resistance is 10% greater than the tip-island resistance) with linear extrapolation to the radius of the tip used in the C-AFM experiments (25 nm). . 19

3.1 Schematic of our C-AFM set-up, with a topography map of a 40 nm x 40 nm area on an atomically flat HOPG terrace recorded by a conductive diamond tip in contact mode. The RMS roughness of the scanned area is ∼0.5 Å. 23

3.2 Comparison of histograms of ECR values obtained from *I*-*V* spectroscopy curves recorded under different conditions: (a) Pt tip under ambient conditions with no control over humidity and temperature, (b) conductive diamond tip under dry N_2 atmosphere at a controlled temperature of 38 °C, with sample degassing performed prior to the experiments (the solid red line is a Gaussian fit), and (c) Pt tip under dry N_2 atmosphere with no control over temperature and no sample degassing. Comparison of (a) and (c) shows that the switch to the dry N_2 environment plays a vital role in reducing the variability of measured ECR values. No normal load other than the adhesion force acted between the tip and the sample in all measurements shown here. 25

3.3 Two experimental runs showing the variation of ECR over (a) ∼30 minutes and (b) ∼15 minutes after contact has been established between tip and sample. The time between two consecutive data points is 3.6 s. The dashed arrows guide the eyes through the initial drop (yellow), followed by spontaneous jumps between different ECR "branches" (red) and periods of nearly constant ECR (black). The gap in data around the 6-minute mark in (a) is due to unstable *I*-*V* curves recorded after the spontaneous jump from which ECR values could not be extracted. 27

3.4 Variation of ECR over ∼4 hours after contact has been established between tip and sample, under an applied normal load of 30 nN. The time difference between two consecutive data points is 3.6 s. After the initial drop (yellow), the absence of spontaneous jumps between different ECR "branches" over several hours (black) is noticeable. . 28

4.1 AFM topography image of (a) an as-cleaved HOPG substrate showing long and wide terraces and, (b) the sample after two-step synthesis of gold islands on HOPG showing the damaged substrate. 31

4.2 A schematic showing the components of a typical thermal evaporator. 32

4.3 AFM topography images showing the results of the one-step synthesis approach with different deposition parameters: (a) substrate temperature: 39 °C, filament current: 45 A and deposition time: 1-2 s, (b) substrate temperature: 300 °C, filament current: 56 A and deposition time: 4-5 s and, (c) substrate temperature: 275 °C, filament current: 50 A and deposition time: 1-2 s. 33

4.4 SEM image showing (a) the distribution of gold islands formed over an area of $\sim$40 μm and (b) the morphology of properly crystallized gold islands. 35

4.5 An AFM topography image showing multiple islands on a single HOPG terrace, with contact sizes ranging from $\sim$40 nm to $\sim$80 nm, highlighted by the black dotted rectangle. 35

LIST OF TABLES

2.1 Total resistance measured on pairs of gold islands via C-AFM, arranged in three data sets acquired on different days. The island-HOPG resistance for small islands is also reported (see Section 2.3.2). Contact radii have been calculated by approximating the island-HOPG contact geometry as circular. For each island, mean and standard deviation values for resistance are deduced from multiple (>10) I-V curves recorded on multiple (>2) spots. 16

Chapter 1

INTRODUCTION

1.1 Electrical Contact Resistance

"God made the bulk, surfaces were invented by the devil", Nobel Prize winning physicist Wolfgang Pauli quipped. This was partially due to the fact that there is no surface that is *absolutely* smooth, no matter how flat it may appear to the bare eye. In other words, even a surface that looks exceptionally smooth on macroscopic length scales is rough on small length scales. However, the relevant roughness parameter for a given analysis may vary from one length scale to another. For example, on the micrometer scale, a given surface may exhibit some degree of waviness depending on the surface finish applied to it. Closer inspection on even smaller length scales reveals that the surface consists of nanoscale asperities as depicted in Figure 1.1. When two such surfaces are brought together, the interface consists of a collection of asperity contacts between the mating surfaces. This leads to a real area of contact that is usually several orders of magnitude lower than the *apparent* area of contact. Locations of contact formed at mating asperities of the surfaces forming the interface are also known as "a-spots".When electrical current is allowed to pass through such an interface, its flow is constricted across the "a-spots" [1, 2] as presented by the sketch in Figure 1.2. Such a constriction of electrical current at the "a-spots" gives rise to electrical contact resistance (ECR). ECR is influenced by the size, shape and chemical characteristics of the asperities that are in contact, among other factors [1, 2].

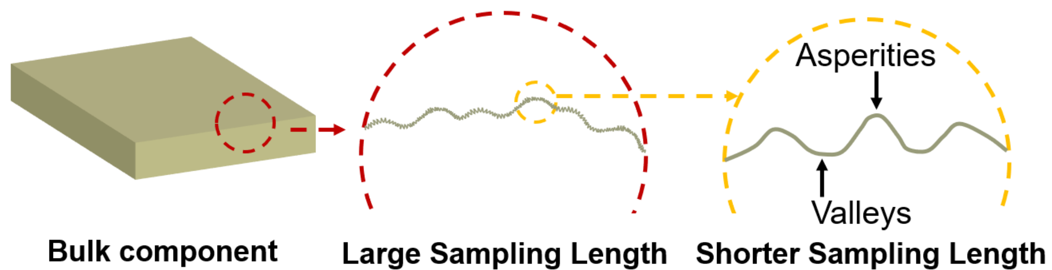

Figure 1.1: Schematic of surface roughness on different sampling lengths.

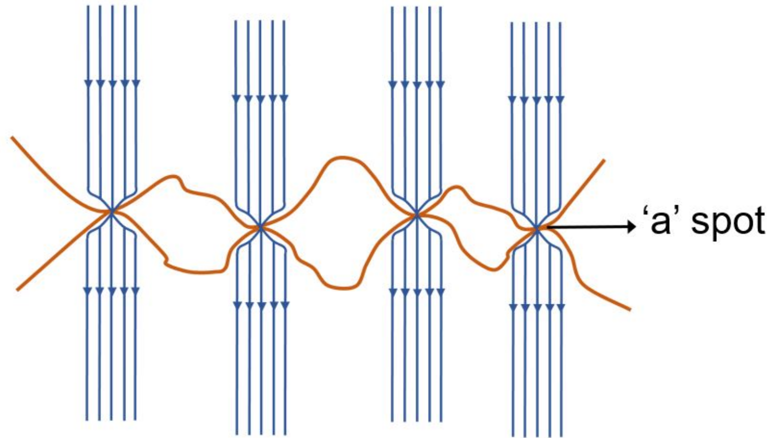

Figure 1.2: A schematic showing constriction of electrical current lines at “a-spots” formed between asperities of two surfaces in contact.

ECR is of crucial importance in the design and performance of electro-mechanical components such as relays, switches and connectors that are employed in many industrial and military applications. In particular, it is crucial to correctly assess ECR for the robust function of micro-electro-mechanical systems (MEMS) due to the fact that surface phenomena become more pronounced at small length scales (see Figure 1.3 for a schematic of a representative MEMS device with electrical contacts) [3]. For instance, while radio frequency (RF) MEMS switches have certain advantages over traditional devices (including highly Ohmic linear contact, low insertion loss, wide bandgap and high cut-off frequency), many of these properties are directly influenced by ECR [4–6]. ECR is also an important design criterion in the emergent research field of low-power integrated circuits to be used in digital logic and memory applications [7]. Various bonding techniques applied in electrical systems such as flip-chip bonding and resistance spot welding also require precise measurement of ECR. For example, low ECR is preferred for flip-chip bonding [8] whereas resistance spot welding benefits from Ohmic heating generated by relatively high ECR values [9]. ECR also plays an important role in the field of tribology. For instance, variation of ECR at an interface during sliding motion can be used as an indicator for tribofilm formation [10]. More specifically, ECR can be a characteristic marker for the transition from static to kinetic friction at the slider-disk interface of a magnetic hard disk [11].

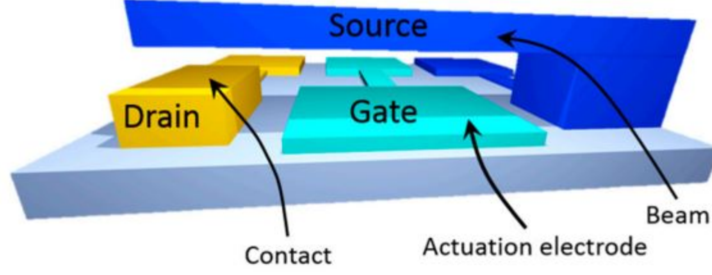

Figure 1.3: Schematic of a representative MEMS device with electrical contacts. Figure from Ref. [7].

The physical mechanisms of ECR can be considered in three regimes based on the relative size of the contact with respect to the electron mean free path in the contacting materials: diffusive regime, ballistic regime and intermediate regime [2]. In situations where the size of the contact is significantly larger than the electron mean free path, diffusive transport of electrons occurs across the interface. The model that describes ECR in the diffusive regime was derived by Maxwell from Ohm's law as

$$R_{Maxwell} = \frac{\rho}{2a} \tag{1.1}$$

where $R_{Maxwell}$ is the ECR in diffusive regime, ρ is the electrical resistivity of the contact and a is the contact radius. ρ can be calculated as the arithmetic average of the electrical resistivities of the contacting bodies. According to Equation 1.1, ECR is inversely proportional to *contact radius* in the diffusive regime. On the other hand, when the contact size is significantly smaller than the mean free path of the involved electrons, ballistic transport occurs. ECR in the ballistic regime is given by Sharvin's equation as

$$R_{Sharvin} = \frac{4\rho\lambda}{3\pi a^2} \tag{1.2}$$

where $R_{Sharvin}$ is the ECR in ballistic regime, and λ is the electron mean free path. According to Equation 1.2, ECR is inversely proportional to *contact area* in the ballistic regime. Finally, when the contact size in on the order of the electron mean free path, ECR falls into the intermediate regime. Wexler proposed a model for ECR in the intermediate regime as [12]:

$$R_{Wexler} = \Gamma(\frac{\rho}{2a}) + \frac{4\rho\lambda}{3\pi a^2} \tag{1.3}$$

where Γ is a function of λ/a, which varies from 1 to 0.694.

It has been revealed via several numerical studies that in micro-scale devices, the individual contact sizes are in the sub-micron regime, i.e. from a few 10s of nm to a few 100s of nm [13]. This means that electron conduction in such devices occurs in the intermediate regime between the diffusive and ballistic limits. However, experimental studies revealed that ECR in the intermediate regime deviates from that predicted by the Wexler model [13]. Therefore, there is an active research effort to develop a better model for ECR in the intermediate regime, preferably through experimental data.

In summary, ECR is an important physical characteristic that plays crucial roles in many fields of science and technology. Even though there has been extensive research effort to study ECR, there is still a lot of room for forming a better understanding of its fundamental mechanisms, particularly on small length scales. Last but not least, it is also crucial to understand how various factors such as contact size, shape and chemistry affect ECR for optimized design of small-scale electro-mechanical systems.

1.2 Atomic Force Microscopy

The invention of scanning probe microscopy (SPM) in the last century opened the doors of the nanoworld to scientists. SPM allows the study of surfaces with unprecedented resolution, down to the atomic scale. The two most common classes of SPM include the Scanning Tunneling Microscope (STM) and the Atomic Force Microscope (AFM). In 1981 Binnig and Rohrer invented the first STM which earned them the Nobel Prize in Physics in 1986, in just 5 years. STM was developed based on the concept of quantum tunneling [14]. In STM, an atomically sharp conductive tip is brought into very close proximity ($\sim$1 nm or below) of the sample surface to be studied, typically under ultra-high vacuum (UHV) conditions. Upon the application of a bias voltage, electrons tunnel through the vacuum, resulting in tunneling current which is a function of tip-sample distance and bias voltage. As the tip scans over the sample surface in a raster fashion, it records a 3-dimensional (3D) topographic map of the sample surface with atomic resolution based on the tunneling current signal. STM is also frequently used to measure local density of states of a given sample and to manipulate atoms [15, 16]. However, the major drawback associated with STM is that the sample has to be electrically conductive. In 1986 the invention of AFM did not only overcome this drawback but also allowed the study of a large number of surfaces with nano- to atomic-scale resolution. AFM operates based on the interatomic forces acting between a very sharp tip and the sample surface [17]. An AFM tip scans over the sample surface in a raster fashion similar to an STM tip and can record topographic, electrical, chemical and magnetic signals with high resolution. While scanning an area as small as 5 nm x 5 nm with AFM under appropriate conditions and using appropriate modes can reveal the atomic structure of a material [18], the method can also be used to probe the

nanomechanical properties of samples such as human cells [19]. AFM also has the capability to operate in a wide variety of environmental conditions such as ambient, UHV, and liquid medium. Another important advantage of AFM is that it can be easily integrated with other instruments for multiple analyses. All these flexibilities have made AFM a very powerful and widely used research tool in many branches of science and technology including physics, chemistry, materials science, and nanoengineering.

1.2.1 General Operating Principle of AFM

AFM is a unique type of microscope in the sense that it does not generate an image through optical and electronic means; instead it's a mechanical microscope that 'touches' the sample with a very sharp tip and generates a 3D image that contains topographical information regarding the surface down to sub-nanometer resolution. The main components of an AFM are a piezo scanner, a cantilever with a very sharp tip at the end that acts as the force sensor and control electronics. The piezo scanner made of piezoelectric material is used to move the tip at the end of the cantilever relative to the sample. The scanning speed of an AFM is limited by the resonant frequency of the piezo electric scanner; in general, the higher the resonant frequency, the faster the scanning speed. Most modern AFM cantilevers are microfabricated with a reflective coating on the top side and a very sharp tip at the end. As the tip rasters over the sample, the cantilever bends due to the changes in the interatomic forces between the tip and the sample caused by topographic variations. A laser beam is focused on the top side of the cantilever and the reflection of the laser beam on a photodiode records the deflection signal of the cantilever. A schematic showing some of the main components of an AFM is shown in Figure 1.4. In typical operation, the electronics (i) record the cantilever deflection signal, (ii) generate signals for the piezo scanner movement using a feedback loop with a PID controller that typically aims to keep the interaction force (as inferred from the cantilever deflection) constant during scanning, and (iii) display/save the recorded topography signal (as inferred from the piezo scanner movement in the vertical direction) in the desired format. An optical microscope is also usually integrated with the AFM to help locate areas of interest on the sample surface and position the laser beam precisely on the backside of the cantilever.

An AFM can be operated in a variety of *modes*. These modes not only differ in the experimental procedure but also record different types of information. Suitability of a mode also greatly depends on the nature of the sample. Some common modes of operation of an AFM are discussed below.

1.2.2 Contact-Mode AFM

In order to understand contact mode operation of AFM, it is important to think about the nature of tip-sample interaction forces as shown in Figure 1.5.

When the tip is far away from the sample surface, it does not interact with the sample surface and therefore the cantilever is at the zero deflection state. As the tip approaches the sample surface, it first experiences attractive forces (e.g. due to van der Waals interactions) and the cantilever bends towards the sample. This is the

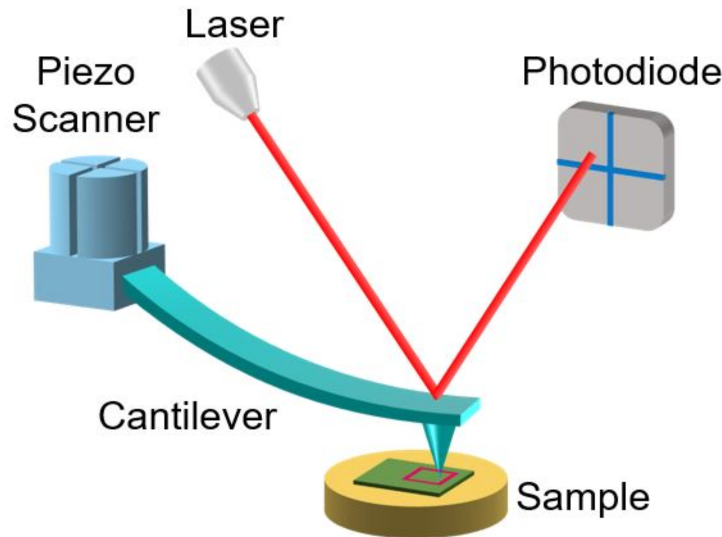

Figure 1.4: Schematic of a typical AFM.

so-called attractive regime. As the distance between the tip and the sample decreases, the attractive force increases and eventually the tip *snaps* into the surface when the rate of change of the attractive force with distance is higher then the deflection stiffness of the cantilever. If the tip is further pushed towards the surface, the cantilever experiences repulsive forces and bends in the opposite direction (i.e. away from the surface). Contact mode AFM is operated in this repulsive regime and is the most straightforward of all topographic imaging modes since the deflection of the cantilever is directly correlated to the topography of the sample. A schematic of contact mode AFM is shown in Figure 1.6 (a). A feedback loop adjusts the position of the cantilever base with respect to the sample by moving the piezo scanner in the vertical (z) direction so that the cantilever deflection is at a constant value. Even though contact mode is capable of generating topographical images with nm-scale lateral resolution, it has several disadvantages; for instance, since the tip operates in the repulsive regime, it can damage soft samples during imaging as there is a shearing (i.e. lateral) force between the tip and the sample at all times. Furthermore, in contact mode, the tip apex can easily become blunt which prevents atomic resolution imaging.

1.2.3 Dynamic Modes of AFM

To overcome some of the limitations associated with contact mode AFM, *dynamic* modes of AFM have been developed. In dynamic mode AFM, the cantilever is oscillated at/near its resonant frequency at a very close proximity to the sample (with average separations on the order of ∼1 nm). As the oscillating cantilever scans over the sample surface, the oscillation amplitude and frequency change via changes in the tip-sample interaction forces, which may be induced by topographical features. Like the contact mode, a feedback loop is used to adjust the z height of the cantilever base such that either the amplitude or the frequency of the oscillation is kept constant. Depending on in which interaction regime the tip is operated, dyna-

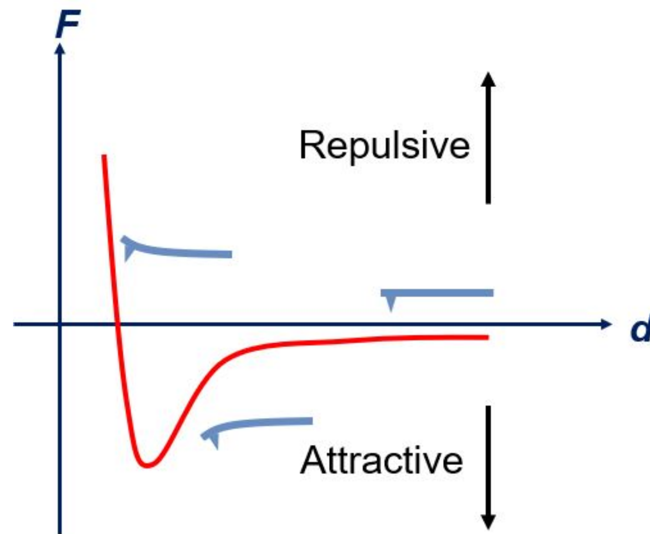

Figure 1.5: Schematic of tip-sample interaction force (F) as a function of separation distance (d).

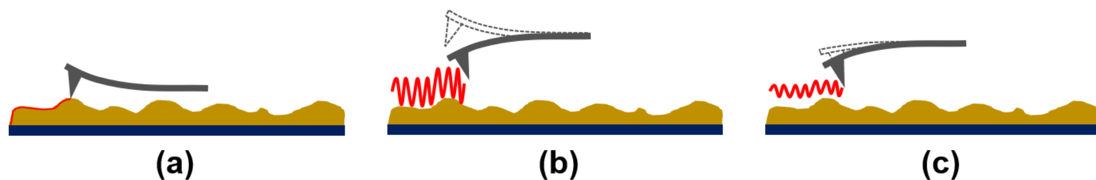

Figure 1.6: Different operational modes of AFM: (a) contact mode, (b) intermittent contact (i.e. tapping) mode and (c) non-contact mode.

mic mode can be classified either as intermittent contact (i.e. tapping) mode or non-contact mode. In non-contact mode, a small oscillation amplitude is applied to

the tip so that it is always in the attractive regime. Non-contact AFM is frequently employed to study crystallographic structures with atomic resolution, due to the possibility of maintaining the atomic sharpness of tips during entire measurements. On the other hand, in the intermittent contact mode, a larger oscillation amplitude is employed such that for each oscillation cycle the tip comes into contact with the sample (i.e. "taps on it") and then goes back, rapidly moving between the attractive and repulsive interaction regimes. Schematics of intermittent contact and non-contact mode AFM are shown in Figure 1.6 (b) and (c), respectively. The primary advantages of dynamic mode AFM are decreased tip and sample damage due to the absence of lateral forces and increased spatial resolution (for non-contact mode).

1.2.4 Force Spectroscopy via AFM

In addition to being a very powerful imaging tool, AFM can also be operated in the so-called spectroscopic mode to perform "force spectroscopy". In particular, the AFM tip is approached to and then retracted from the sample surface in a controlled fashion on a given position, while the interaction force, inferred from the cantilever deflection, is recorded. This results in the measurement of force-distance (F-d) curves (directly related to interatomic force interactions) that can be used to study various mechanical properties of the sample such as stiffness and therefore Young's modulus, adhesion forces etc.

1.3 Conductive Atomic Force Microscopy

Conductive atomic force microscopy (C-AFM) is an important AFM-based technique where a conductive AFM tip is employed to investigate the electrical properties of a given sample. C-AFM is frequently utilized in both imaging and spectroscopic modes. In C-AFM imaging mode, a conductive tip scans the sample surface in contact mode i.e. in the repulsive regime under the application of a bias voltage between the tip and the sample. Such scans provide both the topographic and conductivity maps of the sample surface with nanometer scale spatial resolution simultaneously. The two data maps are independently acquired as topographic information is obtained from cantilever deflection whereas conductivity information is recorded via the amount of current flow through the conductive tip. Moreover, in C-AFM, the tip can be fixed at a given position on the sample surface and current can be recorded as a function of the applied bias, which is known as current-voltage (I-V) spectroscopy. The method of C-AFM has been extensively used to study a multitude of sample systems since its first demonstration in the early 1990s [20, 21]. One of the first C-AFM studies was performed to measure local dielectric properties of silica/silicon oxide, a vital component of very large scale integration (VLSI) devices [22]. C-AFM had significant contributions to the development of nanoelectronics. For example, C-AFM has been used not only for electrical characterization

of carbon nano tube (CNT) transistors but also to induce defects on CNTs and study the resulting changes in electrical properties [23, 24]. Furthermore, it has been employed to study layer-by-layer dielectric break down of 2D materials [25], perform local photolithography via anodic oxidation [26], and study resistive switching behavior of metal-insulator-metal junctions [27]. Other nanostructures that have been studied via C-AFM include quantum dots, nanowires, nanowire-based transistors etc. [28–31]. With C-AFM, one can also probe mechanical and electrical properties simultaneously by recording F-d and I-V curves [32]. Such studies can provide information about the physical characteristics of the contact formed between the tip and the sample. Finally, C-AFM has also been extensively employed to study the electrical properties of molecular tunnel junctions in the last decade with the underlying hope of developing nanoscale circuits based on the nonlinear I-V characteristics of molecules [33].

The key component of a C-AFM experiment is the conductive tip. In general, different types of conductive tips are commercially available such as metal coated tips, conductive diamond coated tips, whole metal body tips etc. C-AFM experiments are highly sensitive to the structure and chemistry of the tips and different tips are suitable for different types of experiments. While metallic tips can be made with sharp apexes ($<$ 25 nm), conductive diamond coated tips typically have larger radii of curvature. Diamond coated tips also have higher resistivity compared to metal coated tips. Even though metallic tips have low resistivity which can be a desirable property for most C-AFM experiments, exposure to ambient conditions usually leads to the formation of an oxide or organic contamination layer on top of the tip apex. It also should be considered that metallic tips wear out much faster than diamond tips and that they tend to mechanically deform during the course of most measurements. Therefore, it is essential to choose the proper tip for a given C-AFM experiment.

1.4 Research Objectives

Even though there have been extensive research efforts aimed at the measurement of ECR at nanoscale via C-AFM for the reasons outlined in Section 1.1, the measured ECR values can so far only be related to approximate contact areas derived from continuum mechanics-based contact models [34], which are known to break down at length scales approaching the atomic regime [35]. In addition, ECR measurements are subject to low reliability and reproducibility due to a number of factors including variations in surface roughness, environmental conditions and tip apex deformation that cannot be quantified *in situ*. Motivated in this fashion, the present thesis has two primary objectives. First, in order to relate ECR to *true* (i.e. real/not apparent) contact areas, the measurement of ECR at sub-micron-sized, atomically flat interfaces formed between a highly oriented pyrolytic graphite (HOPG) substrate and gold islands is demonstrated. Moreover, efforts

aimed at establishing an improved C-AFM methodology are reported that lead to much lower standard deviations in measured ECR data when compared with conventional C-AFM measurements. Finally, an improved sample preparation approach is presented. In summary, the studies reported here (i) open the doors for forming concrete connections between the physical properties of contact (such as its true size and shape) and ECR and (ii) provide the means for more reliable collection of ECR data, with implications for the improved design and development of small-scale electro-mechanical systems.

1.5 Thesis Outline

This thesis consists of five chapters. In Chapter 1, the key subjects of electrical contact resistance and atomic force microscopy are introduced, which is followed by an overview of research objectives.

In Chapter 2, a proof-of-concept approach for correlating ECR to true, measurable contact areas is presented by measuring ECR at atomically flat interfaces formed between an HOPG substrate and gold islands via C-AFM. The experimental findings are complemented by molecular dynamics (MD) simulations performed by the group of Ashlie Martini at UC Merced. This chapter also highlights certain limitations of the sample system associated with the preparation method.

In Chapter 3, an improved C-AFM methodology leading to more reliable ECR data acquisition is presented. In particular, this chapter comprises C-AFM experiments performed on bare HOPG as a model system under controlled environmental conditions.

In Chapter 4, an improved approach to synthesize gold nano islands on HOPG is demonstrated that overcomes the limitations discussed in Chapter 2. Moreover, future plans to study the physical mechanisms of ECR on this improved sample system are briefly introduced.

Finally, in Chapter 5 a brief summary of the thesis is presented with a concise outline for future work.

Chapter 2

ELECTRICAL CONTACT RESISTANCE AT ATOMICALLY FLAT INTERFACES

2.1 Electrical Contact Resistance and Contact Area

As discussed in detail in Chapter 1, ECR plays an important role in the function and performance of small-scale electro-mechanical devices and C-AFM is a powerful and widely used technique to measure ECR. Having said this, despite the relatively wide-spread use of the method, there are significant drawbacks associated with conventional C-AFM measurements. First, wear of the tip apex during extended periods of scanning, especially when trying to achieve large contact sizes by applying large normal loads, can cause resistance measurements to change over time [36]. Second, potential oxidation and/or contamination of the tip and the sample during the experiments can lead to lower-than-expected current flow across the interface [32, 37, 38]. Third, nanoscale roughness of the tip and/or sample result in true conductive contact areas that are much smaller than the apparent size of the contact. Lastly, lack of information about the geometry of the contact established between the AFM tip and the substrate requires that contact size be approximated using continuum-based contact mechanics models which may break down at the nanoscale [34, 35, 39]. All of these hinder the ability to correlate conduction and resistance measured using traditional C-AFM directly to contact size, which in turn limits the formation of a complete understanding of trends observed in such measurements.

There have been research efforts to address the issues discussed above. For example, recent studies employed C-AFM on a sample system with micro-fabricated Pd/Au disks of 100-500 nm radius on an HOPG substrate [40–42]. During the experiments, the metal-coated tip of the AFM cantilever was "welded" onto a particular metal contact and I-V curves were measured to characterize electrical resistance. While such an approach is advantageous as the size of the contact can be directly measured via AFM, the roughness as well as the degree of molecular cleanliness at the interface between the Pd/Au disks and the HOPG remain uncharacterized, which prevents unambiguous correlations to be made between the measured resistances and true conductive contact areas. Perhaps more importantly, the experiments were limited to one measurement per island since the tip was welded to the

disk prior to testing, preventing measurements to be made on contacts of different size with the same probe.

Motivated as above, in this part of the thesis, we present an approach that leverages the concept of measuring conductance at nanoscale contacts, where the true contact size is known and multiple measurements of conductance at different contacts can be performed with the same probe. Specifically, the contact of interest is formed by nanoscale gold islands of varying size on HOPG. As the interface that is formed between the gold islands and HOPG has been shown to be atomically flat and molecularly clean following a specific method of preparation [43], these junctions represent an ideal scenario where ECR can be fundamentally studied, without ambiguities associated with contact geometry and cleanliness encountered in conventional C-AFM experiments. Proof-of-principle experiments introduced here are complemented by molecular dynamics (MD) simulations that enable explicit control of island and tip size as well as approximation of electrical current. Importantly, the simulations provide guidance for the tip and island sizes needed to effectively implement this method for studies of ECR at nanoscale contacts.

2.2 Materials and Methods

A two-step process was followed to synthesize the gold islands on HOPG. First, ZYB-quality HOPG samples (Ted Pella) were cleaved in air and rapidly introduced into the vacuum chamber of a thermal evaporator (Denton Vacuum), where they were covered with a thin layer of 99.999% purity gold for a total deposition amount of 1 Å. The gold-covered HOPG samples were then annealed in a bench-top furnace at a temperature of 650 °C for 120 min. The resulting sample system consisted of individual, crystalline gold islands of varying lateral (up to ∼400 nm) and vertical (up to ∼90 nm) size on the HOPG substrate (Figure 2.1). The wide variation in the lateral size of the gold islands, which are known to exhibit atomically flat and molecularly clean interfaces with the HOPG substrate [43],is particularly advantageous for the experiments proposed here, as it allows ECR to be studied directly as a function of true contact size, overcoming a major limitation of conventional C-AFM experiments.

Once sample preparation and characterization via scanning electron microscopy (SEM) were complete, the sample was imaged via tapping-mode AFM (Asylum Research, Cypher VRS) to locate individual gold islands of interest for I-V spectroscopy (see, e.g., the two islands of different size on the same HOPG terrace highlighted in Figure 2.2). In addition to the fact that AFM imaging allows a precise determination of the area of contact formed between individual gold islands and the HOPG substrate, it can also be employed to determine the island height and to evaluate topographical roughness on the top surface of gold islands (which was measured to be 3.0 ± 1.3 Å (mean ± s.d.) for our sample system), potential factor

that could cause variations in I-V curves obtained on different spots on a given gold island.

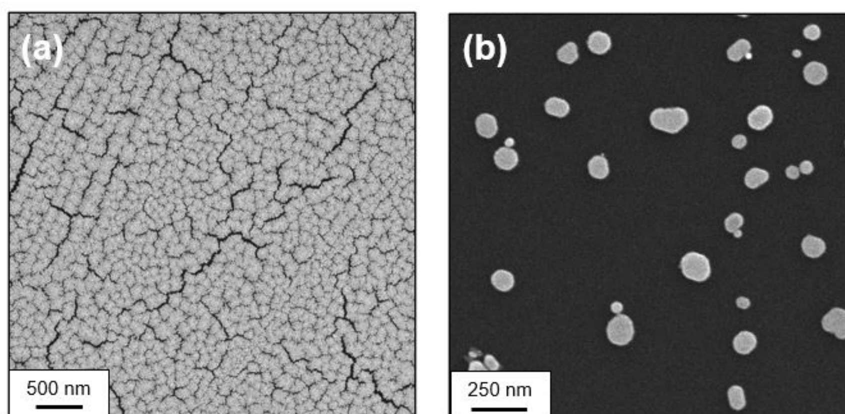

Figure 2.1: Representative SEM image of (a) thin gold film thermally evaporated on freshly cleaved HOPG, (b) the sample system consisting of gold islands of varying size on HOPG, obtained via annealing of the sample in (a).

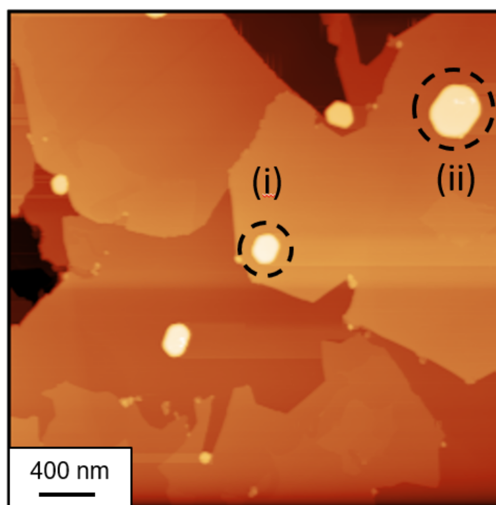

Figure 2.2: AFM image of several gold islands on HOPG. Two gold islands (of size 34,800 nm^2 and 111,900 nm^2) on which I-V measurements were performed are highlighted with dashed circles and indicated as (i) and (ii), respectively.

Following AFM imaging, a Ti/Ir-coated conductive cantilever (Asylum Research, ASYELEC.01-R2, tip radius of ∼25 nm as confirmed by SEM imaging) was

brought into contact with the surface of individual gold islands at desired locations. *I-V* spectroscopy (whereby the bias voltage was applied to the conductive cantilever) was then performed to assess the electrical conductance across the multijunction contact formed by the tip apex, the gold island, and the HOPG substrate (which is electrically connected to the AFM sample plate via silver paint). The majority of measured *I-V* curves were of Ohmic character around zero bias, with a mostly linear dependence of current on bias voltage. It should be mentioned here that such Ohmic measurements of current as a function of bias voltage were not obtained with all conductive AFM tips, and "blocking" behavior (that involves essentially no current flow up to several volts of bias voltage) was also occasionally observed [32]. For tips that exhibited Ohmic behavior, the total resistance (R_{Total}) was determined by linear fits to the data around zero bias. As proof-of-principle experiments, multiple *I-V* curves were collected on individual spots on gold islands of varying size, in a bias voltage range of -7.0 mV to +7.0 mV and a small applied normal load of 0.5 nN (it should be noted that for this particular tip, adhesion on the gold islands was on the order of 10.0 nN).

2.3 Results and Discussion

2.3.1 Correlation between Island Size and Total ECR

Figure 2.3(a) shows five *I-V* curves measured consecutively (over a total span of ~2 min) on an individual spot on island (i) identified in Figure 2.2 which has an area of 34,800 nm^2, demonstrating high reproducibility. The variability of measurements taken at different spots on a given island was also tested. Figure 2.3(b) presents representative *I-V* curves collected on five different spots separated by a few tens of nanometers on island (i) that demonstrate noticeable variation, such that R_{Total} (as deduced from a total of 28 curves collected on five different spots) for this particular island was determined to be 93.8 ± 19.2 kΩ. Moreover, Figure 2.3(c) shows five *I-V* curves collected on five different spots (again separated by a few tens of nm) on another gold island (which is designated as island (ii) in Figure 2.2 and has an area of 111,900 nm^2), on the same terrace as island (i). R_{Total} for island (ii), (again, as deduced from a total of 28 curves collected on five different spots) was measured as 40.2 ± 1.2 kΩ. As expected, a smaller total resistance was measured on the larger island because of the lower resistance at the island-HOPG junction.

The resistance measurements described above were repeated with two additional pairs of islands with significantly different size, with each pair located on the same HOPG terrace. All measurements were performed with the same tip and at an applied normal load of 0.5 nN, and repeat measurements performed on the first island after the collection of *I-V* curves on both islands were utilized to rule out the potential occurrence of tip changes during the experiments. The results of each set of experiments, summarized in Table 2.1, consistently demonstrated a larger R_{Total}

for smaller islands. Note that, while the results for two islands in a given data set can be compared, resistances cannot be compared across the data sets because the islands are on different terraces and HOPG terraces have been reported to exhibit significant differences in resistance [44].

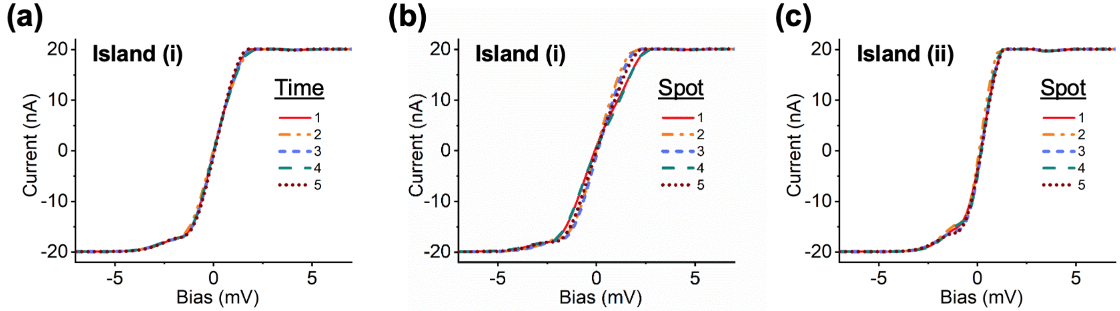

Figure 2.3: (a) Five I-V curves obtained on an individual spot on island (i) in Figure 2.2 over a duration of 2 min., demonstrating high reproducibility. Note that the current saturates at 20.0 nA, which is the limit of our measurement setup. (b) Five I-V curves obtained on five different spots on island (i) in Figure 2.2, demonstrating noticeable variability. (c) Five I-V curves obtained on five different spots on island (ii) in Figure 2.2, demonstrating less variability than those obtained on island (i). Please note the larger slope of the I-V curves on island (ii) when compared with island (i), indicative of a smaller resistance to electron flow, in accordance with the larger size of the island.

Interestingly, the larger islands in the three data sets in Table 2.1 all exhibited very similar R_{Total} values (40.2 ± 1.2 kΩ, 43.3 ± 5.1 kΩ, and 40.1 ± 1.1 kΩ), despite significant differences in the contact size (111,900 nm^2, 130,900 nm^2, and 61,900 nm^2, respectively). On the other hand, mean R_{Total} values measured on the smaller islands were appreciably different from each other (93.8 ± 19.2 kΩ, 73.4 ± 16.9 kΩ, and 56.1 ± 9.7 kΩ). Also, a particularly interesting observation here was that the standard deviation of R_{Total} on smaller islands was significantly higher than that on larger islands. A potential explanation could involve the superlubric nature of the contact between the gold islands and the HOPG substrate and the associated miniscule barriers to motion experienced by small islands [43], supported by the observation that the smaller islands tended to move laterally on the HOPG substrate during the collection of I-V curves.

Data Set	Island size (nm^2)	Island radius (nm)	Total resistance (kΩ)	Island-HOPG resistance (kΩ)
I	111,900	189	40.2 ± 1.2	
	34,800	105	93.8 ± 19.2	53.6 ± 19.2
II	130,900	204	43.3 ± 5.1	
	16,500	72	73.4 ± 16.9	30.1 ± 17.7
III	61,900	140	40.1 ± 1.1	
	23,000	86	56.1 ± 9.7	16.1 ± 10.2

Table 2.1: Total resistance measured on pairs of gold islands via C-AFM, arranged in three data sets acquired on different days. The island-HOPG resistance for small islands is also reported (see Section 2.3.2). Contact radii have been calculated by approximating the island-HOPG contact geometry as circular. For each island, mean and standard deviation values for resistance are deduced from multiple (>10) *I-V* curves recorded on multiple (>2) spots.

2.3.2 Extracting the ECR at the Island-HOPG Junction

To provide explanations for the findings described above, MD simulations were performed by the group of Ashlie Martini at UC Merced, mimicking the C-AFM experiments as shown in Figure 2.4. The model consisted of a diamond-like carbon (DLC) tip apex in contact with gold islands on an HOPG substrate [Figure 2.4(a)]. Three different tips with radii of 3.6, 4.1, and 5.0 nm were brought in contact with gold islands of varying contact areas ranging from 50 to almost 2400 nm^2. The HOPG substrate consisted of two graphene layers having lateral dimensions of 10 x 10, 25 x 20, or 48 x 40 nm^2, depending on the size of the island (lateral size of the HOPG substrate did not affect results). The bottommost graphene layer was fixed and the topmost part of the tip was treated as a rigid body. A normal load of 1.25 nN was applied to the tip. The simulations were performed in the canonical ensemble with the LAMMPS code [45]. The atomic configurations were visualized using OVITO [46]. The Embedded-Atom Method (EAM) [47] was used to model Au-Au interactions and the Adaptive Intermolecular Reactive Empirical Bond Order (AIREBO) [48] potential was used for C-C interactions. The interactions between materials were modeled using the Morse potential for Au-C (D_0 = 0.00832 eV, r_0 = 0.387035 nm, and α = 1.25707) [49]. The time step was 1 fs. For each island and tip combination (three tips and twelve islands), equilibration was run until the system reached steady state, defined as the point at which the vertical position of the top rigid part of the tip varied by less than 0.1 Å, which took up to 450 ps. After this point, production simulations were run for another 100 ps, from which atomic configurations were extracted at 0, 25, 50, 75, and 100 ps for use in the current calculations.

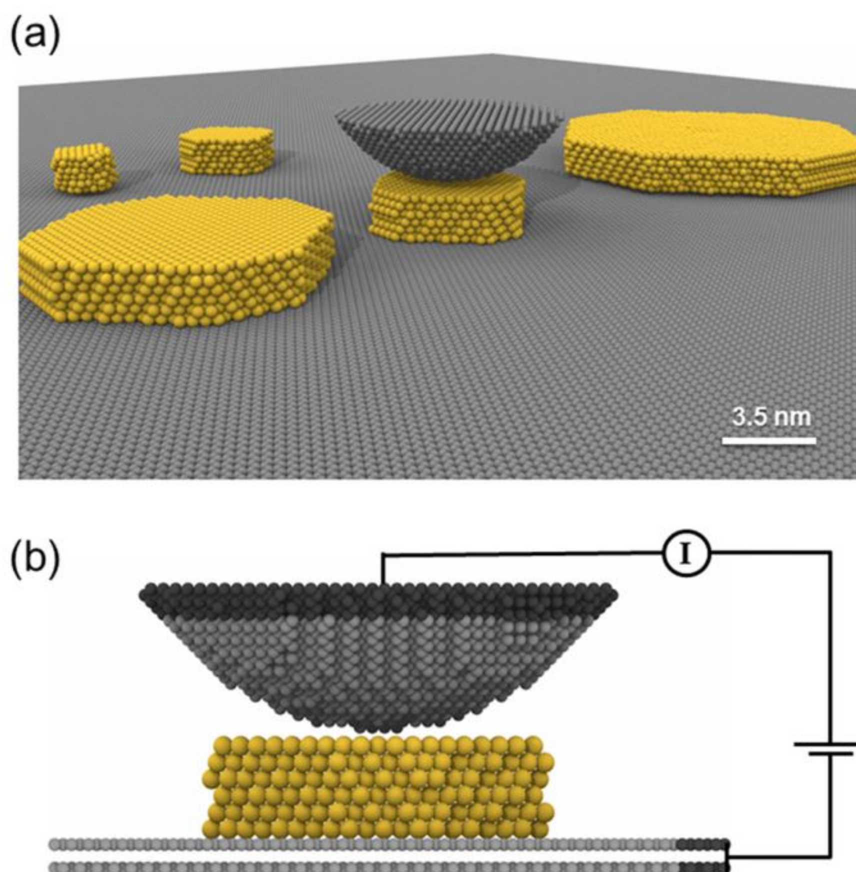

Figure 2.4: (a) Perspective view of the MD simulations where a model AFM tip apex comes into contact with gold islands of varying size on a graphite substrate. (b) For each tip-island combination, current between the tip and the edge of the graphite substrate (shown in darker gray) is approximated using the EChemDID method.

For each tip-island combination, the EChemDID [50] method was used to estimate the current between the top of the tip and edge of the graphite, as shown in Figure 2.4(b). This method has been successfully used before to study the behavior of nanoswitches [51, 52] and C-AFM measurements [53, 54]. EChemDID requires the use of a reactive potential, so for the current calculations, the potential for all interatomic interactions was changed to ReaxFF, with parameters for systems containing gold and carbon atoms [55, 56]. The atomic configurations taken from the production simulations with the nonreactive potential were used as the starting point for the EChemDID calculations. Note that this approach was used because the large model sizes precluded direct use of ReaxFF for the simulations.

For each configuration, EChemDID was run to calculate current and then the average was taken from the five configurations for each tip-island combination. Although EChemDID inherently assumes diffusive transport, this is reasonable for the relatively large island-HOPG contacts modeled here based on an analysis of carrier transport in graphene-metal junctions [57]. Furthermore, any error associated with this assumption for the smaller tip-island contacts is the same for all the models and so will not affect the trends predicted by the simulations.

The results of the total resistance calculated from simulations of three different tips and twelve different islands are shown in Figure 2.5. For this model system, if we assume that the resistance within the tip, the island, and the HOPG is small compared to that at the two interfaces, the total resistance is

$$R_{Total} = R_{Tip} + R_{Tip-Island} + R_{Island} + R_{Island-HOPG} + R_{HOPG} \tag{2.1}$$

$$R_{Total} \approx R_{Tip-Island} + R_{Island-HOPG} \tag{2.2}$$

Therefore, the resistance observed in Figure 2.5 is due to both tip-island and island-HOPG junctions. For large islands, resistance will be dominated by the much smaller tip-island contact, which does not change with the island size, consistent with the near-constant resistance observed for larger islands in Figure 2.5. For small islands, the island-HOPG contact contributes appreciably to the total resistance, leading to total resistance values that decrease with increasing island size, again as observed in Figure 2.5. For each tip, the resistance-island size data were fit to an exponential function that captured the decrease in resistance with increasing island size for small islands (where both tip-island and island-HOPG resistances contribute) and the constant resistance for large islands (where tip-island contact resistance is dominant). We then identified the island radius corresponding to a total resistance that is 10% greater than the tip-island resistance and assumed this to be the maximum island size for which the total resistance can be differentiated from the tip-island resistance. Using the maximum island size calculated for three model tips, we linearly extrapolated to the tip size range relevant for the experiments, as shown in the inset of Figure 2.5. For the 25 nm radius tips employed in C-AFM experiments, this analysis suggested that island radii smaller than 101 nm would be needed to feasibly extract the island-HOPG contact resistance from the measured total resistance. Although the choice of 10% here is arbitrary, other reasonable choices yield similar results, e.g., the maximum island size for the 25 nm tip with a 20% criterion is 75 nm.

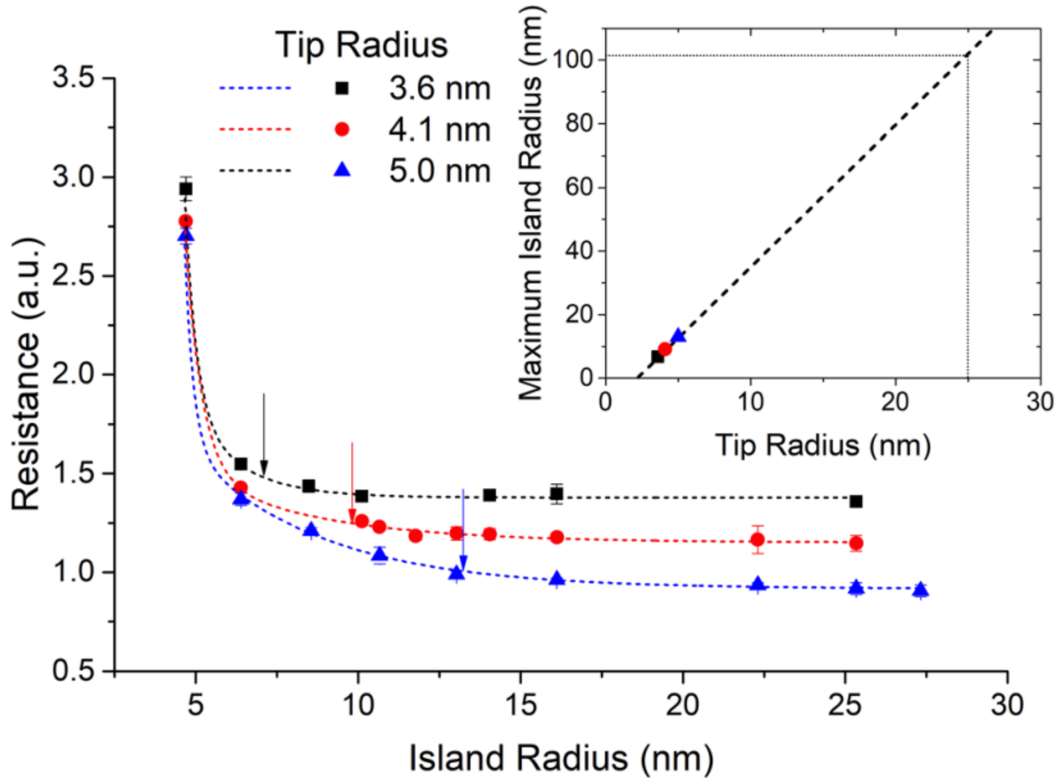

Figure 2.5: Total resistance calculated from the simulations as a function of island radius for three different model tips (symbols). The data are fit to an exponential function (dashed lines) to determine the maximum island radius for each tip (arrows), after which the contribution of the island-HOPG resistance to the total resistance becomes negligible (see the text). Inset: Maximum island radius for each model tip (considering island radii where the total resistance is 10% greater than the tip-island resistance) with linear extrapolation to the radius of the tip used in the C-AFM experiments (25 nm).

The simulation results have significant implications for the C-AFM method reported here: they explain the observation of very similar resistance values for large islands in our experiments, despite significant differences in the size, in contrast to smaller islands where the contribution of the island-HOPG resistance to the total resistance is appreciable. In particular, our experimental results summarized in Table 2.1, when interpreted with the help of MD simulations, point toward a tip-island resistance value on the order of 40 kΩ (as deduced from the measurements on the larger islands in the three datasets, where the contribution of the island-HOPG junction to the measured resistance is negligible). Taking the resistor-in-series model

into account, the resistance measured on the big islands can then be subtracted from the resistance measured on smaller islands in each data set, thereby allowing the calculation of the electrical contact resistance at the island-HOPG junction for the smaller islands (see the last column of Table 2.1). Again, these numbers cannot be compared with each other because the islands are on different terraces [44]. Finally, the largest island-HOPG contact radius for which the contribution of the island-HOPG junction to the total resistance can be detected was determined to be 105 nm in our experiments (Table 2.1), reasonably close to the range extrapolated from the MD simulations (75 to 101 nm).

While the results reported above indicate that measurements should be performed on smaller islands to accurately determine ECR at island-HOPG interfaces, an alternative and/or complementary approach could involve the use of tips with large radii, such that the resistance of the tip-island junction is minimized and the relative contribution of the island-HOPG resistance to the total resistance increases. This could, for instance, be achieved by the deliberate blunting of tips prior to the experiments [58, 59] or the use of conductive colloidal probes. These avenues can be pursued in future research.

2.4 Summary

In summary, this chapter of the thesis demonstrated an approach to C-AFM aimed at enabling direct correlations between the true contact size and ECR. The approach leveraged the well-defined, atomically flat contact that forms between gold islands and HOPG. Proof-of-principle experiments were supplemented by MD simulations that approximated resistance for model systems in which the exact sizes of both tip-island and island-HOPG contacts were known. The simulations explained the experimental findings that showed a trend of an increasing contribution of the island-HOPG junction to the measured total resistance with decreasing island size. The approach demonstrated here has the potential to contribute to a fundamental understanding of electron conduction mechanisms at small length scales, for instance by enabling an investigation of the transition between the diffusive and ballistic electron transport regimes, which constitutes a main direction that will be followed in future work.

Chapter 3

IMPROVING THE RELIABILITY OF ECR MEASUREMENTS

3.1 Reliability of ECR Measurements

Despite the significant role that ECR information provided by C-AFM can play in the design of small-scale electro-mechanical systems [60–62], the method has suffered from reliability and reproducibility issues since its first utilization in the 1990s [20, 21]. This is mainly due to the fact that the resistance to electron conduction at the nanoscale tip-sample junction is highly susceptible to changes in chemistry as well as surface structure. Such changes can be induced by varying environmental conditions, including temperature and humidity, and facilitated by the chemical reactivity of the tip and sample materials as well as their mechanical characteristics. A quantitative evaluation of some factors leading to sizeable variances in C-AFM measurements was presented earlier [34], and results demonstrated that ECR could vary by at least an order of magnitude in a single experimental run.

Attempts were made to improve the reliability and reproducibility of C-AFM measurements by changing the tip material. While metallic or metal-coated tips typically used for C-AFM (e.g. Pt, Pt/Ir and Ti/Ir tips) have the desirable property of low resistivity, they suffer from wear and are susceptible to oxide formation which leads to inaccuracies in the measurement of surface electrical properties [32]. On the other hand, while conductive diamond tips are highly wear resistant, hard to deform and do not form oxide layers under ambient conditions, they have significantly higher resistivities and larger radii of curvature than metallic and metal-coated tips, leading to a reduction in current and spatial resolution. The topographical roughness of the sample itself also affects the reproducibility of C-AFM measurements: during repeated measurements on a rough sample, the AFM tip may land on areas of different local roughness, which would consequently lead to differences in effective contact area and thus, ECR. Finally, environmental conditions influence the reliability of ECR measurements to a great extent. Under uncontrolled ambient conditions, oxidation of the tip and sample, the presence of adsorbates, and changes in humidity and temperature can lead to a very high standard deviation in measured ECR values [34]. These issues can be overcome by performing experiments under ultra-high vacuum (UHV) conditions, but metallic tips wear easily in UHV due to the lack of a lubrication layer formed by adsorbates [37].

Motivated by the above, in this part of thesis we present an approach to improve the reliability of ECR measurements via C-AFM by addressing multiple sources of variability. Specifically, we perform ECR measurements on atomically flat terraces of HOPG via *I-V* spectroscopy using conductive diamond tips under an inert nitrogen (N_2) environment and at closely controlled temperatures. The atomically flat HOPG surface eliminates the impact of sample roughness variations on measured ECR values. The use of diamond tips minimizes complexities related to tip wear and deformation. Before starting measurements, the HOPG sample is annealed under N_2 to desorb contaminants. The ECR measurements performed in this fashion exhibit significantly lower standard deviation than those obtained using conventional measurement conditions. Finally, even under ideal conditions, we observe spontaneous changes in ECR values during measurements extending over several minutes. However, application of a higher normal load is shown to be one way to suppress these changes. Overall, the approach reported here constitutes a well-defined route towards more reliable ECR measurements by C-AFM.

3.2 Materials and Methods

The improved C-AFM measurements were performed on ZYB-quality HOPG samples (Ted Pella) that were cleaved using the Scotch Tape method under ambient conditions and immediately inserted into the controlled environment of the sample chamber in a commercial AFM (Asylum Research, Cypher VRS). A constant flow of dry N_2 gas through the sample chamber was maintained overnight to purge ambient gases and achieve an inert N_2 atmosphere. Under the N_2 environment, the HOPG sample was heated at 100 °C for 60 minutes to desorb adsorbates from the sample surface. The degassed HOPG sample was then allowed to cool to a temperature of 38 °C, which was maintained stable ($\pm$ 0.1 °C) throughout the experiments with a built-in sample heater via PID control.

In this stable environment, relatively small areas (40 nm x 40 nm) on the HOPG surface were scanned in contact mode using either Pt tips (HQ:NSC18/Pt, μmasch) or conductive diamond tips (CDT-CONTR, Nanosensors), on an atomically flat terrace without step edges in close proximity. A schematic of the C-AFM set-up along with a representative topography map are shown in Figure 3.1. The representative area presented in Figure 3.1 is atomically flat, with an RMS roughness of $\sim$0.5 Å, thus eliminating the effect of sample roughness variations on the reproducibility of measurements. To extract ECR values, consecutive *I-V* spectroscopy measurements (in a "vertical" C-AFM setup [63]) were performed on such regions of the HOPG sample over varying periods of time (from a few minutes to a few hours). ECR values were extracted from the slope of the linear region of each *I-V* spectroscopy curve with an applied bias voltage ranging from -100 to 100 mV. The majority of experiments were performed with no applied normal load other than the

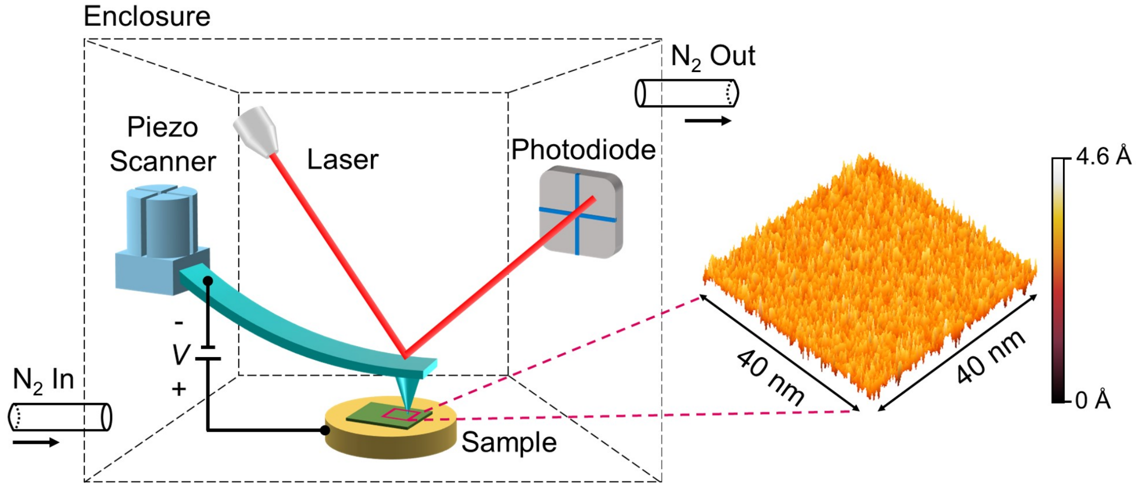

Figure 3.1: Schematic of our C-AFM set-up, with a topography map of a 40 nm x 40 nm area on an atomically flat HOPG terrace recorded by a conductive diamond tip in contact mode. The RMS roughness of the scanned area is ∼0.5 Å.

adhesion force, which was found to be, via force-distance spectroscopy, in the range of 20 to 30 nN for conductive diamond tips and around 10 nN for Pt tips. The surface was imaged before and after force-distance spectroscopy experiments to verify that there was no damage to the HOPG substrate.

3.3 Results and Discussion

3.3.1 Comparison between Conventional and Improved ECR Measurements

To determine the extent to which the precautions discussed above (the use of wear-resistant and mechanically strong conductive diamond tips, suppressing fluctuations in environmental humidity and temperature, as well as degassing the sample before the measurements) have improved the reliability of C-AFM-based ECR measurements, we performed comparative experiments, the results of which are summarized in Figure 3.2.

In particular, Figure 3.2(a) is a histogram of the measured data that demonstrates the spread of ECR values measured on a single location on a flat HOPG terrace under ordinary laboratory conditions (i.e. with no control over humidity and temperature) over a span of 70 minutes using a Pt tip. As one can clearly observe from the presented data, ECR values recorded in this fashion (extracted from 1157 individual I-V curves) vary dramatically, over more than an order of magnitude, reminiscent of the results presented by *Engelkes et al.* in their detailed

study of ECR variations [34]. In addition to the variance in the recorded ECR values, the absolute values (with a mean ECR of 2.45 MΩ and a standard deviation of 2.95 MΩ) are significantly higher than what would be expected from a nanoscopic contact formed between a Pt tip and HOPG (which is on the order of a few kΩ to tens of kΩ [2]), pointing towards the potential presence of contaminant layers on the probe and/or the sample [38, 64–66].

In contrast to Figure 3.2(a), Figure 3.2(b) presents results (extracted from 1200 individual *I*-*V* curves recorded over 70 minutes) that were obtained by taking all the precautions described in Section 3.2, i.e. with a conductive diamond tip, under an N_2 atmosphere and a controlled temperature of 38 °C, with degassing of the HOPG sample performed prior to the *I*-*V* spectroscopy experiments. The data obtained in this fashion are in striking contrast to those presented in Figure 3.2(a): ECR values now exhibit a much narrower distribution that can be fit reasonably well with a Gaussian, with a mean of 18.6 MΩ and a standard deviation of only 0.90 MΩ. While the absolute values of the ECR are higher than those obtained via the Pt tip, this can be tentatively attributed to the fact that the resistivity of the conductive diamond is expected to be at least two orders of magnitude higher than the resistivity of platinum [67, 68].

While it is obvious from the comparison of the data in Figure 3.2(a) and Figure 3.2(b) that the combined measures of using a hard and wear-resistant tip material and controlling environmental factors have led to a dramatic improvement in reliability, it is not possible to determine which precaution had the most significant impact on the improvement of the data. To address this question, we repeated our C-AFM-based ECR measurements with the Pt tip one more time, but now under an inert N_2 atmosphere, albeit with no control of temperature or sample degassing (Figure 3.2(c)). The data (extracted from 1200 individual *I*-*V* curves recorded over 70 minutes) now exhibit a significantly more narrow distribution (with a mean of 98.0 MΩ and a standard deviation of 12.6 MΩ) than what was achieved under ambient conditions in Figure 3.2(a).

Despite the fact that the variability in ECR measurements observed via the use of Pt tips under the dry N_2 atmosphere (Figure 3.2(c)) is still appreciably higher than what is achievable with the conductive diamond tips (Figure 3.2(b)), the drastic improvement after the switch from ambient conditions to N_2 highlights the major impact that environmental conditions and, in particular, changes in humidity can have on C-AFM-based ECR measurements. On the other hand, at first glance it may be surprising that the mean ECR measured with the Pt tip (98.0 MΩ) is higher than the ECR measured with the conductive diamond tip (18.6 MΩ). This difference, however, can be explained by the fact that (i) a degassing procedure was

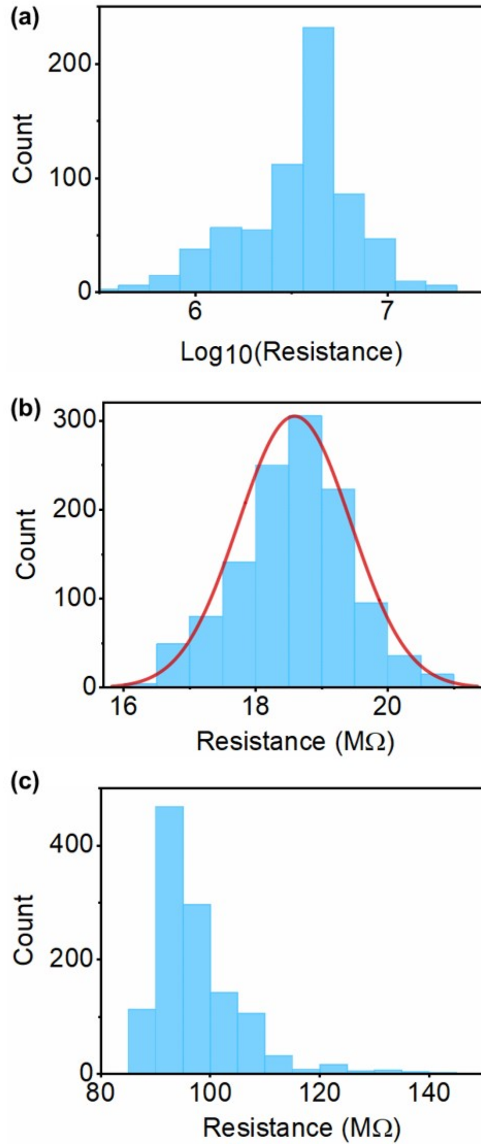

Figure 3.2: Comparison of histograms of ECR values obtained from I-V spectroscopy curves recorded under different conditions: (a) Pt tip under ambient conditions with no control over humidity and temperature, (b) conductive diamond tip under dry N_2 atmosphere at a controlled temperature of 38 °C, with sample degassing performed prior to the experiments (the solid red line is a Gaussian fit), and (c) Pt tip under dry N_2 atmosphere with no control over temperature and no sample degassing. Comparison of (a) and (c) shows that the switch to the dry N_2 environment plays a vital role in reducing the variability of measured ECR values. No normal load other than the adhesion force acted between the tip and the sample in all measurements shown here.

not used for the measurement with the Pt tip and (ii) the measurements were not taken at the same location on the same terrace and different HOPG terraces can exhibit significantly different conductivities [44].

While experiments reporting on the variability of C-AFM-based ECR measurements and the underlying mechanisms are quite rare in the literature [34, 69, 70], it is still possible to consider our results within the context of these studies. In particular, for C-AFM measurements performed on decanethiol-coated gold substrates, it was reported that the resistance values obtained in a single experimental run with a given AFM tip varied by upto three orders of magnitude, depending on the topographical roughness of the gold substrate employed in the experiments [34]. Moreover, switching from measurements in air to those performed under cyclohexane (analogous to the switch from ambient conditions to the dry N_2 atmosphere in our experiments) minimized the issues associated with uncontrolled changes in humidity, leading to a drastic decrease in standard deviation [34]. Another study focusing on a similar material system (self-assembled monolayers of azobenzene thiol molecules on gold) reported results along the same lines, with resistance values varying over more than an order of magnitude [70]. Finally, C-AFM measurements on a granular gold film resulted in resistance values that varied over two orders of magnitude, and the authors attributed the large variability in the results to atomic re-arrangements and mechanical instabilities at the tip-sample junction [69]. The ECR distributions achieved via our improved methodology (see e.g. Figure 3.2(b)) are significantly more narrow than those reported in the discussed experiments [34, 69, 70], possibly due to the combined use of mechanically strong AFM tips and strictly controlled environmental conditions.

3.3.2 Spontaneous Changes in ECR Measurements

Despite the improvements in reliability reported in Section 3.3.1, we have observed that at least one source of variability remains. In particular, when measurements are continuously performed for durations of a few minutes and longer (with all the precautions described earlier), spontaneous (i.e. sudden) changes in ECR can be observed. Figure 3.3 presents two experimental runs (performed with conductive diamond tips for ∼30 minutes and ∼15 minutes after contact has been established between tip and sample) that comprise spontaneous jumps to different "branches" of ECR as highlighted by the red arrows. Specifically, in Figure 3.3(a), after an initial gradual drop, the ECR spontaneously jumps to a lower branch, stays stable for about 2 minutes and then jumps back to the value before the spontaneous drop. The ECR then remains fairly stable for about 12 minutes, which is then followed by another spontaneous drop. In the second experimental run presented in Figure 3.3(b), there is no initial drop, but the data shows a prominent downward jump in ECR at the ∼3 minute mark, followed by a stable region for about 9 minutes and then another downward jump of smaller magnitude.

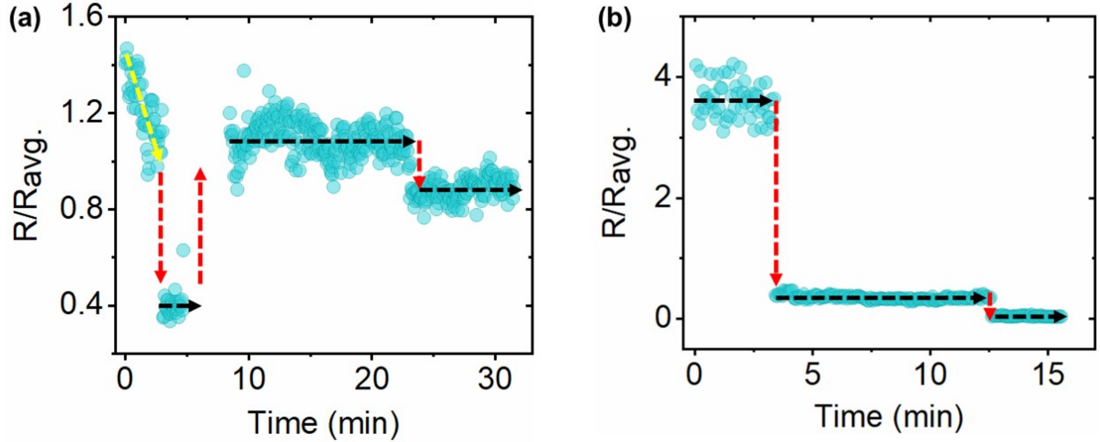

Figure 3.3: Two experimental runs showing the variation of ECR over (a) ∼30 minutes and (b) ∼15 minutes after contact has been established between tip and sample. The time between two consecutive data points is 3.6 s. The dashed arrows guide the eyes through the initial drop (yellow), followed by spontaneous jumps between different ECR "branches" (red) and periods of nearly constant ECR (black). The gap in data around the 6-minute mark in (a) is due to unstable *I*-*V* curves recorded after the spontaneous jump from which ECR values could not be extracted.

While the initial gradual drop in resistance in Figure 3.3(a) can be tentatively explained by creep [71], the spontaneous jumps in Figure 3.3(a) and (b) appear to be of a different character. During C-AFM measurements, the tip-sample junction is subject to the combined effects of electrically-, thermally-, and mechanically-induced stresses [72]. While, the flow of current through the constricted tip-sample junction leads to Joule heating [73] and consequently thermal stresses, the junction also undergoes electrical stress due to the repeated, cyclic application of bias voltage over an extended period of time to perform *I*-*V* spectroscopy [74], in addition to mechanically-induced stresses though the action of adhesive forces acting between the tip and the sample. The potential influence of piezo creep on the contact should also not be ignored. A mechanism that may explain a sudden drop in ECR is the spontaneous breakdown of an insulating contaminant layer [37]. On the other hand, the rapid increase to higher ECR values cannot be explained through a similar mechanism. As such, an alternative explanation that involves spontaneous changes in the atomic-scale structure of the AFM tip apex, perhaps by the re-positioning of a cluster of atoms near the contact in a metastable configuration [75] can result in the experimentally observed jumps between different ECR branches. Support from atomic-scale simulations will be needed to gain more insight into the underlying physical mechanism.

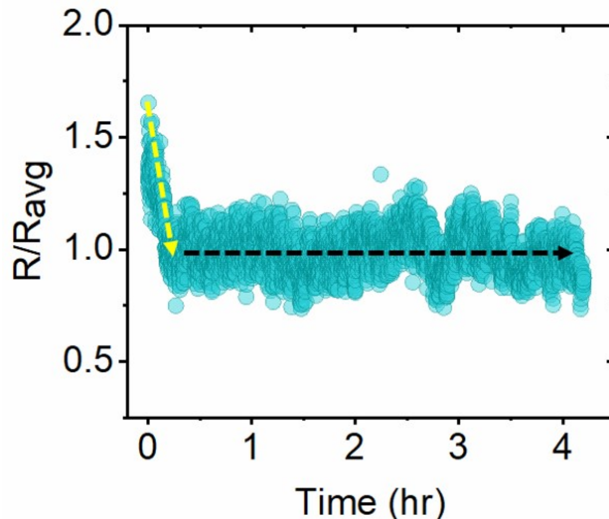

Figure 3.4: Variation of ECR over ∼4 hours after contact has been established between tip and sample, under an applied normal load of 30 nN. The time difference between two consecutive data points is 3.6 s. After the initial drop (yellow), the absence of spontaneous jumps between different ECR "branches" over several hours (black) is noticeable.

Regardless of the underlying mechanisms, in order to explore whether the occurrence of spontaneous jumps in ECR can be minimized through experimental means, we recorded a ∼4-hr-long run with a conductive diamond tip in which I-V curves were continuously recorded under an applied normal load of 30 nN, which is on the same order as the typical adhesion force measured between diamond and HOPG. The results, presented in Figure 3.4, still exhibit an initial gradual drop in ECR, no spontaneous jumps in ECR are recorded subsequently, demonstrating that sudden changes in ECR can be suppressed through the application of normal load at the tip-sample junction. A potential physical mechanism could involve a deepening of potential energy minima for atomic clusters at the tip apex with increasing normal load [76], making it harder for the clusters to jump between different spatial configurations at the apex. The confirmation of this hypothesis would again require input from atomic-scale simulations.

3.4 Summary

An improved approach to C-AFM-based ECR measurements has been presented. The method minimizes the impacts of sample surface roughness, tip deformation and wear, sample contamination, as well as fluctuations in humidity and temperature on the acquired data. The ECR values measured using our approach exhibit a fairly Gaussian distribution with much lower standard deviation than those

obtained under conventional measurement conditions. We have identified that the key factor leading to improved data acquisition was the switch from ambient conditions to a dry N_2 atmosphere. Despite the precautions taken, we still observe spontaneous changes in ECR values over time. While support from atomic-scale simulations is needed to understand the details of the physical mechanisms underlying these changes, it is found that the application of normal load at the tip-sample junction suppresses their occurrence. Overall, the approach reported here represents a significant step towards increasing the reliability of C-AFM measurements.

Chapter 4

IMPROVED SYNTHESIS OF GOLD ISLANDS ON GRAPHITE

4.1 Complexities of Gold Island Synthesis on Graphite

Although the two-step procedure (deposition of a thin film of gold on HOPG, followed by annealing in air) presented in Chapter 2 successfully synthesizes crystalline gold islands on HOPG, several complications arise due to the high temperature annealing step. In particular, metallic gold islands catalytically etch the HOPG substrate at high temperatures, causing structural damage in the form of channels and pits [77]. This results in mainly three drawbacks for C-AFM measurements:

(i) The average HOPG terrace size is significantly reduced compared to the as-cleaved HOPG substrate. Figure 4.1(a) and 4.1(b) show the topography images of an as-cleaved HOPG substrate and an HOPG substrate after annealing at 650 °C as part of the two-step synthesis of gold islands, respectively. The as-cleaved HOPG substrate has wide terraces as shown in Figure 4.1(a). On the other hand, the two-step synthesis of gold islands damages the HOPG substrate as it can be easily seen in Figure 4.1(b), which in turn reduces the chances of finding multiple gold islands on individual HOPG terraces.

(ii) During annealing, the gold atoms making up the deposited film diffuse on the surface and coalesce in the form of gold islands that are stuck in channels and step edges (see, Figure 4.1(b)), which are sub-optimal for our C-AFM measurements where the measurable contact of interest needs to be formed between the bottom surface of the islands and the flat HOPG terraces on which they are located.

(iii) Even if multiple gold islands are found that are located nicely in the middle of individual HOPG terraces away from step edges and other defects, the ECR measured on these islands cannot be compared as different HOPG terraces may exhibit different conductivities [44].

All of these issues hinder our ability to compare ECR measured on gold islands of varying size. To circumvent the aforementioned difficulties, we have developed a one-step approach to synthesize gold islands of a wide size distribution on HOPG without damaging the HOPG substrate. The samples prepared by this improved approach

(i) preserve the structural integrity of the underlying HOPG featuring large terraces,

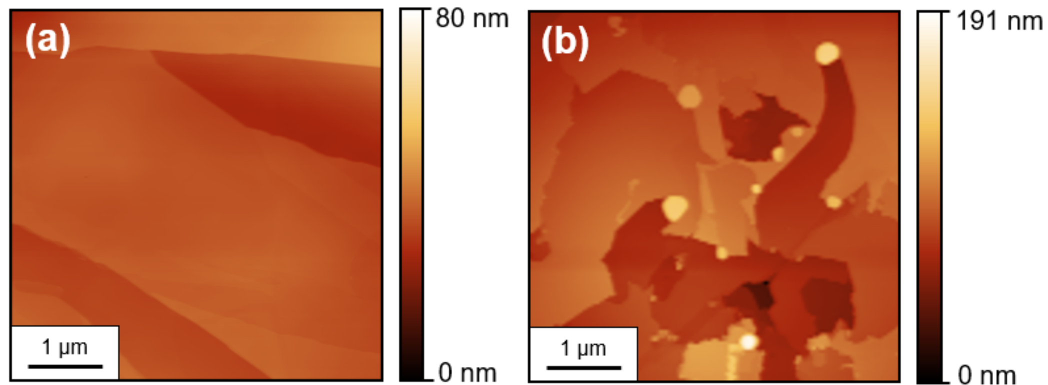

Figure 4.1: AFM topography image of (a) an as-cleaved HOPG substrate showing long and wide terraces and, (b) the sample after two-step synthesis of gold islands on HOPG showing the damaged substrate.

(ii) exhibit a number of crystalline gold islands of varying size on individual HOPG terraces, and

(iii) contain islands with equivalent contact radii that are on the same order or slightly smaller than the electron mean free path in gold, allowing us to study ECR in the intermediate regime in future work.

4.2 Materials and Methods

The one-step synthesis of gold islands on HOPG was performed at the Molecular Foundry at the Lawrence Berkeley National Laboratory, in collaboration with Dr. Paul Ashby. First, ZYB-quality HOPG (Ted Pella) was freshly cleaved via Scotch Tape under ambient conditions and immediately placed inside the evaporation chamber of a thermal evaporator (Denton Vacuum). A schematic of the thermal evaporator is shown in Figure 4.2. During thermal evaporation, the three main parameters that could be optimized were:

1. Substrate temperature (temperature of HOPG substrate during gold deposition),

2. Deposition rate (controlled by the filament current through the gold source), and

3. Deposition time (the amount of time during which gold is being deposited on the sample).

The thermal evaporator is equipped with a halogen heater lamp. Using this lamp, the HOPG substrate was heated at a temperature of 275-300 °C for 120-180 minutes to desorb adsorbed contaminants from the surface under high vacuum conditions (Pressure: 4 x 10^{-6} Torr). After desorbing contaminants, 99.999% purity gold was deposited on HOPG at different substrate temperatures ranging from 39

°C to 300 °C to synthesize gold islands with the desired size and shape distribution. Parameters other than substrate temperature that were changed during the deposition experiments included the deposition rate as controlled by the filament current (which varied from 45 to 56 A) and the deposition time (which was varied from 1 to 6 s). The prepared samples were subsequently imaged via SEM and AFM to optimize deposition parameters.

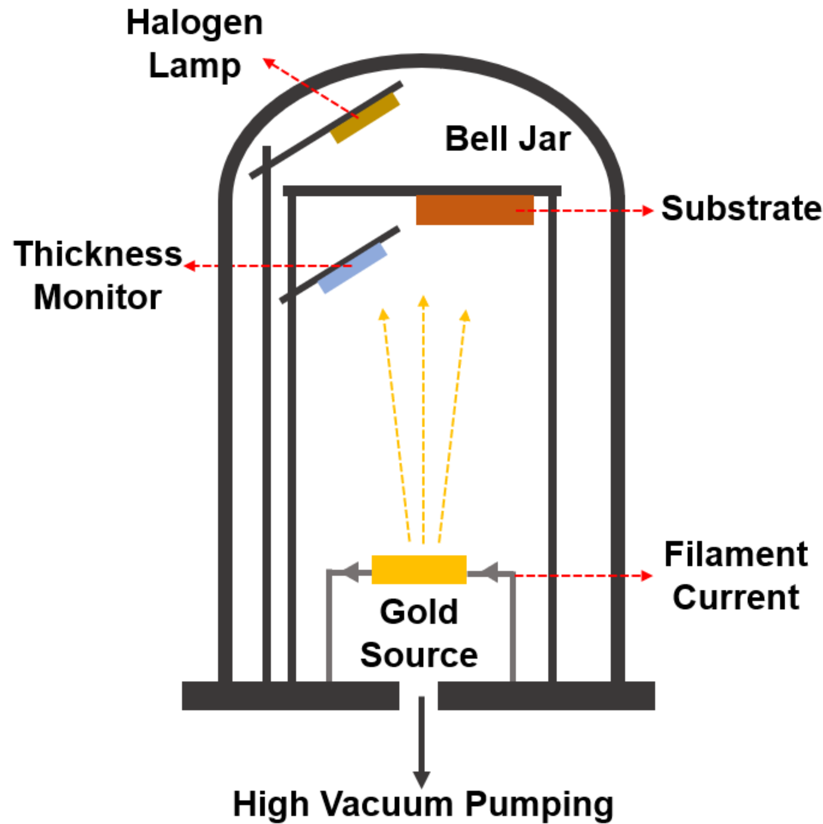

Figure 4.2: A schematic showing the components of a typical thermal evaporator.

4.3 Results and Discussion

4.3.1 Optimizing Synthesis Parameters

One-step synthesis of gold islands on HOPG (ZYA-quality) has been demonstrated by Dietzel *et. al.* [78] by depositing gold on an HOPG substrate kept at room temperature under ultrahigh vacuum conditions. However, we found that depositing gold on a heated HOPG substrate under high vacuum also produces gold islands with a desirable size and shape distribution. In Ref. [78], the authors first heated the HOPG substrate at 150 °C for 30 minutes under UHV conditions to

remove residual contaminants, cooled down the substrate and then evaporated gold at room temperature to synthesize gold islands. In our first attempt, we heated the HOPG at 150 °C for 120 minutes under high vacuum conditions (Pressure: 4 x 10^{-6} Torr) and then cooled it down to a temperature of 39 °C. Subsequently, evaporation of gold was performed with a filament current of 45 A for 1-2 s. Figure 4.3(a) shows an AFM topography image of the sample that was prepared in this fashion. An immediate observation was that this approach sustained the structural integrity of the HOPG substrate. By comparing Figure 4.3(a) with Figure 4.1(b) or Figure 2.2 in Chapter 2, one can easily observe that the terraces of the HOPG substrate were preserved via our one-step approach that avoids post-deposition annealing. However, one can further observe that the deposited gold did not have enough thermal energy to crystallize into well-faceted islands. Therefore, the conclusion was that the substrate temperature needed to be increased to provide enough thermal energy to the evaporated gold atoms to form well-faceted islands. We can further observe from Figure 4.3(a) that almost all the deposited gold migrated to step edges of the HOPG substrate. Therefore, the deposition amount needed to be increased so that there is enough gold to form islands on top of the HOPG terraces away from the step edges. In order to increase the amount of gold deposition, we needed to increase the filament current and deposition time.

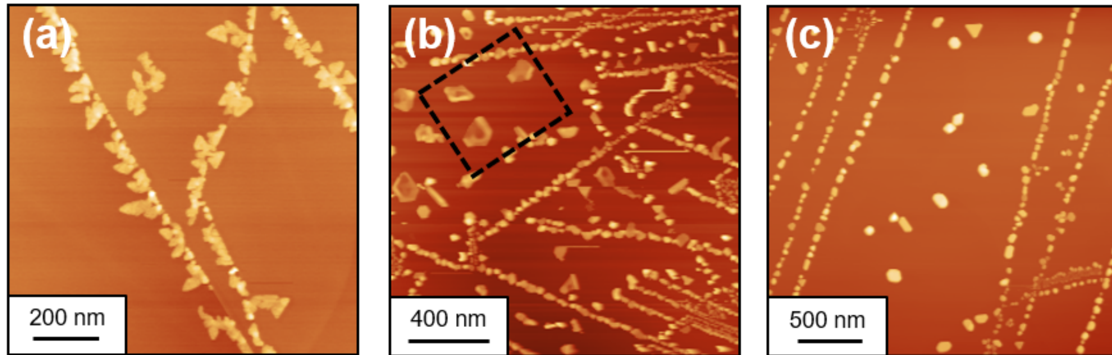

Figure 4.3: AFM topography images showing the results of the one-step synthesis approach with different deposition parameters: (a) substrate temperature: 39 °C, filament current: 45 A and deposition time: 1-2 s, (b) substrate temperature: 300 °C, filament current: 56 A and deposition time: 4-5 s and, (c) substrate temperature: 275 °C, filament current: 50 A and deposition time: 1-2 s.

Consequently, in our next attempt, we heated the HOPG substrate at 300 °C for 180 minutes under high vacuum conditions (Pressure: 4 x 10^{-6} Torr) and evaporated gold on the heated HOPG with a filament current of 56 amp and deposition time of 4-5 s. An AFM topography image of the sample prepared in this

way is shown in Figure 4.3(b). Even though we could see islands formed on top of the HOPG terraces away from step edges as highlighted by the rectangular box in Figure 4.3(b), the structure of the islands was not optimal. The islands appeared multi-faceted which is not ideal for our C-AFM measurements. In addition, while we could find islands of lateral size around a hundred nm and even more, we were lacking a reasonable number of smaller islands of lateral size around a few tens of nm. Therefore, we concluded that the deposition amount needed to be reduced such that we have enough gold to form islands on the HOPG terraces in a lateral size that goes down to a few tens of nm. Furthermore, the substrate temperature needed to be decreased to prevent all of the smaller islands from migrating to step edges of HOPG.

In our following attempt, the HOPG substrate was heated at 275 °C for 180 minutes under high vacuum conditions (Pressure: 4 x 10^{-6} Torr) and evaporation of gold was performed on the heated HOPG with a filament current of 50 A for 1-2 s. An AFM topography image of this sample is presented in Figure 4.3(c). As one can easily observe, crystallized islands of varying size are located on top of HOPG terraces away from step edges. The sample was further imaged via SEM to observe the distribution of islands over larger areas, in particular above 30 μm which is the limit of lateral scan size in our AFM. The SEM image shown in Figure 4.4(a) confirmed the distribution of gold islands of varying size on structurally intact large HOPG terraces. The SEM image in Figure 4.4(b) further confirmed the well-faceted crystalline nature of the gold islands.

4.3.2 Electrical Contact Resistance in Different Conduction Regimes

Depending on the ratio of contact size at the interface to the electron mean free path in the involved materials, electron transport can be ballistic, intermediate or diffusive. Apparent and true contact areas differ by multiple orders of magnitude in general and measuring the true contact area is not straightforward. However, in the special case of atomically flat interfaces, apparent and true contact areas are the same. Following this line of logic, ECR values were correlated to a measurable true contact area by utilizing the atomically flat interfaces formed between gold islands and HOPG substrate in Chapter 2 [79], but the proof-of-principle experiments covered only the diffusive conduction regime where the size of the contact formed between the gold islands and the underlying HOPG were large compared to the electron mean free path in gold (38 nm [80]). The disadvantages associated with the sample preparation technique described in Section 4.1 prevented us from studying the physical mechanisms of ECR across these atomically flat interfaces in the ballistic and intermediate conduction regimes. With the improved synthesis of gold islands on HOPG discussed above, a new avenue opens for us to directly observe

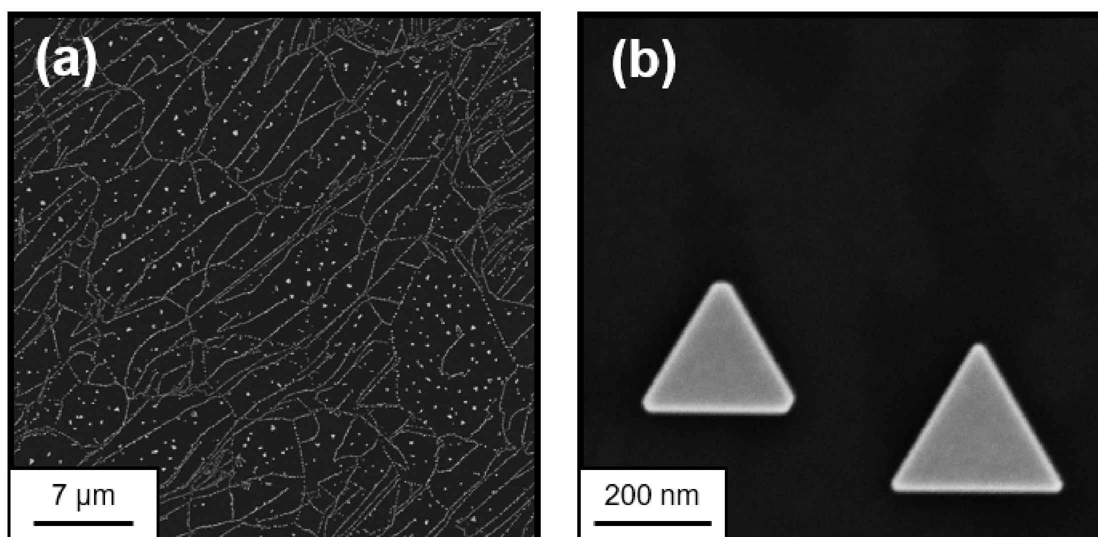

Figure 4.4: SEM image showing (a) the distribution of gold islands formed over an area of ~40 μm and (b) the morphology of properly crystallized gold islands.

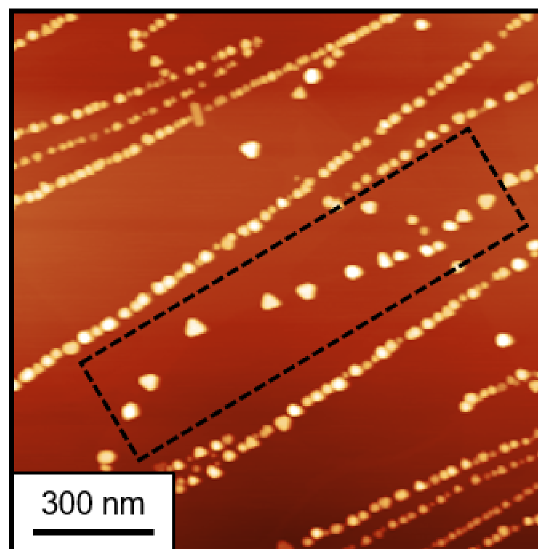

Figure 4.5: An AFM topography image showing multiple islands on a single HOPG terrace, with contact sizes ranging from ~40 nm to ~80 nm, highlighted by the black dotted rectangle.

the transition between the diffusive and ballistic limits of ECR by focusing on islands of different size on the same substrate terrace. Figure 4.5 shows an AFM topography

image where multiple islands on a single HOPG terrace are highlighted with contact size ranging from ~40 nm to ~80 nm. Since the electron mean free path in gold is ~38 nm, the contact sizes of the gold islands shown in Figure 4.5 should at least cover the initial transition into the ballistic regime. As one can see from Figure 4.5, one can even find smaller islands on the sample surface that should exhibit ballistic transport. As the intermediate and ballistic electron transport regimes are relevant for billions of individual contacts that are formed between components in modern small-scale electro-mechanical devices [13], this avenue of research will be pursued further in future work.

4.4 Summary

In this Chapter of the thesis, an improved technique to synthesize gold islands on HOPG has been presented. The improved one-step technique preserves the structural integrity of the underlying HOPG. Consequently, multiple gold islands of varying size form on top of wide HOPG terraces which can be utilized to measure and compare ECR. The optimal substrate temperature for the formation of the gold islands has been found to be 275 °C with an optimal filament current of 50 A and deposition time of 1-2 s. The gold islands formed by this improved technique are highly crystalline and well-faceted with straight edges. The improved sample prepared following this approach will play a crucial role in future work focusing on studying the physical mechanisms of ECR at atomically flat interfaces across the transition from the ballistic to diffusive electron conduction regimes.

Chapter 5

CONCLUSIONS

This thesis focused on measuring electrical contact resistance at sub-micron length scales using the method of C-AFM. The primary measurement tool was a commercial AFM (Asylum Research, Cypher VRS) whereas thermal evaporation and annealing were utilized for sample preparation. In addition, SEM was used for complementary sample characterization.

Even though several experimental studies in the literature measured ECR as a function of contact size (e.g. Ref. [40]), there were ambiguities associated with the structure of the contact and the precise measurement of the contact area. We unambiguously correlated ECR to a *true*, measurable contact area by utilizing atomically flat interfaces formed between two crystalline materials where the real contact area is the same as the apparent contact area. In particular, we synthesized crystalline gold islands on atomically flat terraces of HOPG. Correlation between the ECR values measured in the proof-of-principle experiments and the contact size formed between the gold islands and the HOPG substrate revealed that (i) smaller islands resulted in higher ECR, (ii) above a threshold island size, the measured ECR values were dominated by the AFM tip-island junction resistance whereas below the threshold island size, the measured ECR values were significantly affected by the island-HOPG junction resistance. These findings, reported in Chapter 2, were published in the form of a journal article [79].

Another important achievement presented in this thesis involves a methodology for improving the reliability of ECR measurements conducted via C-AFM. Our improved technique suppresses the effects of tip deformation, humidity and temperature variations, as well as substrate roughness, resulting in ECR values that exhibit significantly smaller variation than those obtained through conventional means [34]. The associated results, presented in Chapter 3, were also published in the form of a journal article [81].

Finally, in Chapter 4, we presented an improved method to synthesize gold islands on HOPG whereby (i) the structural integrity of the HOPG substrate is preserved, (ii) multiple gold islands can be located on individual HOPG terraces away from step edges and, (iii) contact sizes associated with islands formed on individual HOPG terraces partially falls into the intermediate regime between the ballistic and diffusive regimes. Therefore, this improved sample system can be utilized to study

the physical mechanisms of ECR in the intermediate regime between the ballistic and diffusive limits at atomically flat interfaces.

Considering the crucial roles ECR plays in small-scale devices and components, including but not limited to MEMS, low-power-density integrated circuits, metal-insulator-metal junctions, and molecular tunnel junctions, it is important to understand the associated fundamental physical mechanisms and precisely characterize how different inherent and environmental factors affect ECR. Even though the outcomes of this thesis contribute important pieces of information regarding ECR at atomically flat interfaces in the diffusive conduction regime, more research effort is required to study the physical mechanisms in other conduction regimes (i.e. the ballistic and intermediate ones). Therefore, our future work will be focused on observing the transition of ECR across different transport regimes at the atomically flat interfaces formed between gold islands and HOPG, and potentially on other material systems. Last but not least, efforts will be focused on forming a precise characterization of the effects of humidity and temperature on ECR at these atomically flat interfaces, which can strengthen our knowledge base about ECR to a great extent, providing useful information for practical applications.

Bibliography

1. Timsit, S. Electrical contact resistance: properties of stationary interfaces. *Electrical Contacts-1998. Proceedings of the Forty-Fourth IEEE Holm Conference on Electrical Contacts (Cat. No. 98CB36238),* 1–19 (1998).
2. Slade, P. G. *Electrical Contacts: Principles and Applications* (CRC press, 2017).
3. Ma, Q. *et al.* Metal contact reliability of RF MEMS switches. *Reliability, Packaging, Testing, and Characterization of MEMS/MOEMS VI* **6463,** 646305 (2007).
4. Newman, H. S., Ebel, J. L., Judy, D. & Maciel, J. Lifetime measurements on a high-reliability RF-MEMS contact switch. *IEEE Microwave and Wireless Components Letters* **18,** 100–102 (2008).
5. Rebeiz, G. M. *RF MEMS: Theory, Design, and Technology* (John Wiley & Sons, 2004).
6. Daneshmand, M. & Mansour, R. R. RF MEMS satellite switch matrices. *IEEE Microwave Magazine* **12,** 92–109 (2011).
7. Peschot, A., Qian, C. & Liu, T.-J. K. Nanoelectromechanical switches for low-power digital computing. *Micromachines* **6,** 1046–1065 (2015).
8. Oh, K. W. & Ahn, C. H. A new flip-chip bonding technique using micromachined conductive polymer bumps. *IEEE Transactions on Advanced Packaging* **22,** 586–591 (1999).
9. Crinon, E. & Evans, J. The effect of surface roughness, oxide film thickness and interfacial sliding on the electrical contact resistance of aluminium. *Materials Science and Engineering: A* **242,** 121–128 (1998).
10. Komvopoulos, K., Chiaro, V., Pakter, B., Yamaguchi, E. & Ryason, P. Antiwear tribofilm formation on steel surfaces lubricated with gear oil containing borate, phosphorus, and sulfur additives. *Tribology Transactions* **45,** 568–575 (2002).
11. Wang, S. & Komvopoulos, K. Friction force, contact resistance, and lubricant shear behavior at the magnetic head-disk interface during starting. *Journal of Tribology* **119,** 830–839 (1997).

12. Wexler, G. The size effect and the non-local Boltzmann transport equation in orifice and disk geometry. *Proceedings of the Physical Society* **89,** 927 (1966).

13. Majumder, S. *et al.* Study of contacts in an electrostatically actuated microswitch. *Sensors and Actuators A: Physical* **93,** 19–26 (2001).

14. Binnig, G. & Rohrer, H. Scanning tunneling microscopy. *Surface Science* **126,** 236–244 (1983).

15. Niimi, Y. *et al.* Scanning tunneling microscopy and spectroscopy of the electronic local density of states of graphite surfaces near monoatomic step edges. *Physical Review B* **73,** 085421 (2006).

16. Crommie, M. F., Lutz, C. P. & Eigler, D. M. Confinement of electrons to quantum corrals on a metal surface. *Science* **262,** 218–220 (1993).

17. Binnig, G., Quate, C. F. & Gerber, C. Atomic force microscope. *Physical Review Letters* **56,** 930 (1986).

18. Baykara, M. Z. Noncontact atomic force microscopy for atomic-scale characterization of material surfaces. *Surface Science Tools for Nanomaterials Characterization,* 273–316 (2015).

19. Cross, S. E., Jin, Y.-S., Rao, J. & Gimzewski, J. K. Nanomechanical analysis of cells from cancer patients. *Nature Nanotechnology* **2,** 780–783 (2007).

20. De Wolf, P., Snauwaert, J., Clarysse, T., Vandervorst, W. & Hellemans, L. Characterization of a point-contact on silicon using force microscopy-supported resistance measurements. *Applied Physics Letters* **66,** 1530–1532 (1995).

21. Shafai, C., Thomson, D., Simard-Normandin, M., Mattiussi, G. & Scanlon, P. Delineation of semiconductor doping by scanning resistance microscopy. *Applied Physics Letters* **64,** 342–344 (1994).

22. Murrell, M. *et al.* Spatially resolved electrical measurements of SiO_2 gate oxides using atomic force microscopy. *Applied Physics Letters* **62,** 786–788 (1993).

23. Yaish, Y. *et al.* Electrical nanoprobing of semiconducting carbon nanotubes using an atomic force microscope. *Physical Review Letters* **92,** 046401 (2004).

24. Park, J.-Y. Electrically tunable defects in metallic single-walled carbon nanotubes. *Applied Physics Letters* **90,** 023112 (2007).

25. Hattori, Y., Taniguchi, T., Watanabe, K. & Nagashio, K. Layer-by-layer dielectric breakdown of hexagonal boron nitride. *ACS Nano* **9,** 916–921 (2015).

26. Alaboson, J. M. *et al.* Conductive atomic force microscope nanopatterning of epitaxial graphene on SiC (0001) in ambient conditions. *Advanced Materials* **23,** 2181–2184 (2011).

27. Lu, W., Wong, L.-M., Wang, S. & Zeng, K. Effects of oxygen and moisture on the IV characteristics of TiO_2 thin films. *Journal of Materiomics* **4,** 228–237 (2018).

28. Woodside, M. T. & McEuen, P. L. Scanned probe imaging of single-electron charge states in nanotube quantum dots. *Science* **296,** 1098–1101 (2002).

29. Birjukovs, P. *et al.* Electrical characterization of bismuth sulfide nanowire arrays by conductive atomic force microscopy. *The Journal of Physical Chemistry C* **112,** 19680–19685 (2008).

30. Kalinin, S. V. *et al.* Electronic transport imaging in a multiwire SnO_2 chemical field-effect transistor device. *Journal of Applied Physics* **98,** 044503 (2005).

31. Erts, D. *et al.* High density germanium nanowire assemblies: contact challenges and electrical characterization. *The Journal of Physical Chemistry B* **110,** 820–826 (2006).

32. O'shea, S., Atta, R. & Welland, M. Characterization of tips for conducting atomic force microscopy. *Review of Scientific Instruments* **66,** 2508–2512 (1995).

33. Beebe, J. M., Kim, B., Gadzuk, J. W., Frisbie, C. D. & Kushmerick, J. G. Transition from direct tunneling to field emission in metal-molecule-metal junctions. *Physical Review Letters* **97,** 026801 (2006).

34. Engelkes, V. B., Beebe, J. M. & Frisbie, C. D. Analysis of the causes of variance in resistance measurements on metal-molecule-metal junctions formed by conducting-probe atomic force microscopy. *The Journal of Physical Chemistry B* **109,** 16801–16810 (2005).

35. Luan, B. & Robbins, M. O. The breakdown of continuum models for mechanical contacts. *Nature* **435,** 929–932 (2005).

36. Frammelsberger, W., Benstetter, G., Kiely, J. & Stamp, R. C-AFM-based thickness determination of thin and ultra-thin SiO_2 films by use of different conductive-coated probe tips. *Applied Surface Science* **253,** 3615–3626 (2007).

37. Lantz, M., O'Shea, S. & Welland, M. Characterization of tips for conducting atomic force microscopy in ultrahigh vacuum. *Review of Scientific Instruments* **69,** 1757–1764 (1998).

38. Vishnubhotla, S. B. *et al.* Quantitative measurement of contact area and electron transport across platinum nanocontacts for scanning probe microscopy and electrical nanodevices. *Nanotechnology* **30,** 045705 (2018).

39. Jacobs, T. D. & Martini, A. Measuring and understanding contact area at the nanoscale: a review. *Applied Mechanics Reviews* **69** (2017).

40. Koren, E., Knoll, A., Lörtscher, E. & Duerig, U. Meso-scale measurement of the electrical spreading resistance in highly anisotropic media. *Applied Physics Letters* **105,** 123112 (2014).

41. Koren, E., Knoll, A., Lörtscher, E. & Duerig, U. Direct experimental observation of stacking fault scattering in highly oriented pyrolytic graphite mesostructures. *Nature Communications* **5,** 1–6 (2014).

42. Koren, E. *et al.* Coherent commensurate electronic states at the interface between misoriented graphene layers. *Nature Nanotechnology* **11,** 752 (2016).

43. Cihan, E., Ipek, S., Durgun, E. & Baykara, M. Z. Structural lubricity under ambient conditions. *Nature Communications* **7,** 1–6 (2016).

44. Banerjee, S., Sardar, M., Gayathri, N., Tyagi, A. & Raj, B. Conductivity landscape of highly oriented pyrolytic graphite surfaces containing ribbons and edges. *Physical Review B* **72,** 075418 (2005).

45. Plimpton, S. Fast parallel algorithms for short-range molecular dynamics. *Journal of Computational Physics* **117,** 1–19 (1995).

46. Stukowski, A. Visualization and analysis of atomistic simulation data with OVITO–the Open Visualization Tool. *Modelling and Simulation in Materials Science and Engineering* **18,** 015012 (2009).

47. Zhou, X., Johnson, R. & Wadley, H. Misfit-energy-increasing dislocations in vapor-deposited CoFe/NiFe multilayers. *Physical Review B* **69,** 144113 (2004).

48. Stuart, S. J., Tutein, A. B. & Harrison, J. A. A reactive potential for hydrocarbons with intermolecular interactions. *The Journal of Chemical Physics* **112,** 6472–6486 (2000).

49. De la Rosa-Abad, J. A., Soldano, G., Mejıéa-Rosales, S. J. & Mariscal, M. Immobilization of Au nanoparticles on graphite tunnels through nanocapillarity. *RSC Advances* **6,** 77195–77200 (2016).

50. Onofrio, N. & Strachan, A. Voltage equilibration for reactive atomistic simulations of electrochemical processes. *The Journal of Chemical Physics* **143,** 054109 (2015).

51. Onofrio, N., Guzman, D. & Strachan, A. Atomic origin of ultrafast resistance switching in nanoscale electrometallization cells. *Nature Materials* **14,** 440–446 (2015).

52. Onofrio, N., Guzman, D. & Strachan, A. Atomistic simulations of electrochemical metallization cells: mechanisms of ultra-fast resistance switching in nanoscale devices. *Nanoscale* **8,** 14037–14047 (2016).

53. Hu, X., Lee, J., Berman, D. & Martini, A. Substrate effect on electrical conductance at a nanoasperity-graphene contact. *Carbon* **137,** 118–124 (2018).

54. Hu, X. & Martini, A. Atomistic simulations of contact area and conductance at nanoscale interfaces. *Nanoscale* **9,** 16852–16857 (2017).

55. Srinivasan, S. G., van Duin, A. C. & Ganesh, P. Development of a ReaxFF potential for carbon condensed phases and its application to the thermal fragmentation of a large fullerene. *The Journal of Physical Chemistry A* **119,** 571–580 (2015).

56. Järvi, T. T., van Duin, A. C., Nordlund, K. & Goddard III, W. A. Development of interatomic ReaxFF potentials for Au–S–C–H systems. *The Journal of Physical Chemistry A* **115,** 10315–10322 (2011).

57. Xia, F., Perebeinos, V., Lin, Y.-m., Wu, Y. & Avouris, P. The origins and limits of metal–graphene junction resistance. *Nature Nanotechnology* **6,** 179–184 (2011).

58. Vishnubhotla, S. B. *et al.* Matching atomistic simulations and in situ experiments to investigate the mechanics of nanoscale contact. *Tribology Letters* **67,** 97 (2019).

59. Gotsmann, B. & Lantz, M. Quantized thermal transport across contacts of rough surfaces. *Nature Materials* **12,** 59–65 (2013).

60. Rezvanian, O., Zikry, M., Brown, C. & Krim, J. Surface roughness, asperity contact and gold RF MEMS switch behavior. *Journal of Micromechanics and Microengineering* **17,** 2006 (2007).

61. Dadgour, H. F., Hussain, M. M., Cassell, A., Singh, N. & Banerjee, K. Impact of scaling on the performance and reliability degradation of metal-contacts in NEMS devices. *2011 International Reliability Physics Symposium,* 3D–3 (2011).

62. Basu, A., Adams, G. & McGruer, N. A review of micro-contact physics, materials, and failure mechanisms in direct-contact RF MEMS switches. *Journal of Micromechanics and Microengineering* **26,** 104004 (2016).

63. Hussain, S. *et al.* Local electrical characterization of two-dimensional materials with functional atomic force microscopy. *Frontiers of Physics* **14,** 33401 (2019).

64. Enachescu, M., Carpick, R. W., Ogletree, D. F. & Salmeron, M. The role of contaminants in the variation of adhesion, friction, and electrical conduction properties of carbide-coated scanning probe tips and Pt (111) in ultrahigh vacuum. *Journal of Applied Physics* **95,** 7694–7700 (2004).

65. Sirghi, L., Kylian, O., Gilliland, D., Ceccone, G. & Rossi, F. Cleaning and hydrophilization of atomic force microscopy silicon probes. *The Journal of Physical Chemistry B* **110,** 25975–25981 (2006).

66. Chen, R., Vishnubhotla, S. B., Jacobs, T. D. & Martini, A. Simulations of the effect of an oxide on contact area measurements from conductive atomic force microscopy. *Nanoscale* **11,** 1029–1036 (2019).

67. Fujimori, N., Imai, T. & Doi, A. Characterization of conducting diamond films. *Vacuum* **36,** 99–102 (1986).

68. Powell, R., Tye, R. & Woodman, M. J. The thermal conductivity and electrical resistivity of polycrystalline metals of the platinum group and of single crystals of ruthenium. *Journal of the Less Common Metals* **12,** 1–10 (1967).

69. Guo, D.-Z., Hou, S.-M., Zhang, G.-M. & Xue, Z.-Q. Conductance fluctuation and degeneracy in nanocontact between a conductive AFM tip and a granular surface under small-load conditions. *Applied Surface Science* **252,** 5149–5157 (2006).

70. Mativetsky, J. M. *et al.* Azobenzenes as light-controlled molecular electronic switches in nanoscale metal-molecule-metal junctions. *Journal of the American Chemical Society* **130,** 9192–9193 (2008).

71. Rezvanian, O. *et al.* The role of creep in the time-dependent resistance of Ohmic gold contacts in radio frequency microelectromechanical system devices. *Journal of Applied Physics* **104,** 024513 (2008).

72. Brunetto, G. & Martini, A. Atomistic description of coupled thermal-mechanical stresses on a gold/HOPG nanocontact. *Computational Materials Science* **130,** 165–171 (2017).

73. Grosse, K. L., Bae, M.-H., Lian, F., Pop, E. & King, W. P. Nanoscale Joule heating, Peltier cooling and current crowding at graphene–metal contacts. *Nature Nanotechnology* **6,** 287–290 (2011).

74. Takahashi, T. & Kawamukai, T. Phase detection of electrostatic force by AFM with a conductive tip. *Ultramicroscopy* **82,** 63–68 (2000).

75. Ghasemi, S. A. *et al.* Ubiquitous mechanisms of energy dissipation in noncontact atomic force microscopy. *Physical Review Letters* **100,** 236106 (2008).

76. Riedo, E., Gnecco, E., Bennewitz, R., Meyer, E. & Brune, H. Interaction potential and hopping dynamics governing sliding friction. *Physical Review Letters* **91,** 084502 (2003).

77. Campos, L. C., Manfrinato, V. R., Sanchez-Yamagishi, J. D., Kong, J. & Jarillo-Herrero, P. Anisotropic etching and nanoribbon formation in single-layer graphene. *Nano Letters* **9,** 2600–2604 (2009).

78. Dietzel, D., Feldmann, M., Schwarz, U. D., Fuchs, H. & Schirmeisen, A. Scaling laws of structural lubricity. *Physical Review Letters* **111,** 235502 (2013).

79. Vazirisereshk, M. R., Sumaiya, S. A., Martini, A. & Baykara, M. Z. Measurement of electrical contact resistance at nanoscale gold-graphite interfaces. *Applied Physics Letters* **115,** 091602 (2019).

80. Gall, D. Electron mean free path in elemental metals. *Journal of Applied Physics* **119,** 085101 (2016).

81. Sumaiya, S. A., Martini, A. & Baykara, M. Z. Improving the reliability of conductive atomic force microscopy-based electrical contact resistance measurements. *Nano Express* **1,** 030023 (2020).